Investigation of an optimal pulsed jet mixing and combustion in supersonic crossflow

ZHAO, Majie, LI, Qinling <http://orcid.org/0000-0002-7191-9538> and YE, Taohong

Published version

ZHAO, Majie, LI, Qinling and YE, Taohong (2021). Investigation of an optimal pulsed jet mixing and combustion in supersonic crossflow. Combustion and Flame, 227, 186-201.

Copyright and re-use policy

Investigation of an optimal pulsed jet mixing and combustion in supersonic crossflow

Majie Zhao[a], Qinling Li[b] & Taohong Ye[a,*]

[a] Department of Thermal Science and Energy Engineering, University of Science and Technology of China, Hefei, 230027, P.R. China

[b] Department of Engineering and Mathematics/MERI, Sheffield Hallam University, S1 1WB, United Kingdom

Abstract

The enhanced mixing and combustion mechanism of pulsed sonic jet with optimal frequency in supersonic crossflow with a 10° ramp has been investigated using Large Eddy Simulation (LES). The results show that the energetic structures from the barrel shock and shear vortex are further enlarged at the phase of $1/4T_0$ periodically due to the swing forward and backward effect of the bow shock. There coexists clockwise and counter-clockwise rotating shear layer vortex structures in the pulsed jet, while only counter-clockwise rotating shear layer vortex structure is found in the steady case. The mixing process and the flame distribution are significantly affected by these structures of different scales. The reflected shock waves in the transverse jet in supersonic crossflow have strong coupling effects with the heat release rate. The pulsed jet is also found to improve the non-premixed dominant heat release rate, but not the premixed one. The mechanism of enhanced mixing and combustion efficiency relevant to the optimal frequency of 50 kHz is studied with Power Spectral Density (PSD) and wavelet analysis, and it is interesting to notice that the optimal pulsed jet frequency has strong coupling effects with the bow shock swing back and forward frequency, the jet shear layer and barrel shock frequencies (i.e. 50 kHz). However, for the non-pulsed steady case, the bow shock characteristic frequency is found to be 40 kHz, which suggests the optimal pulsed jet frequency

can be 40 kHz. In order to further validate it, Unsteady Reynolds Averaged Navier Stokes (URANS) simulations have been performed with the pulsed jet frequency of 40 kHz. It is optimising to see that the mixing and combustion efficiency are further improved.

***Keyword*:** Scramjet, supersonic combustion, pulsed jet, transverse jet in supersonic crossflow, LES

1 Introduction

In order to unlock the further of space access and hypersonic flights, great efforts have been dedicated to the research and development of hypersonic vehicles in the past decades [1,2]. Within the scramjet engine combustor, the supersonic flow is dynamically compressed through an intake system, and the fuel and oxidizer are burnt under the supersonic condition. Due to an order of a fraction of a millisecond residence time in the supersonic combustor, the dynamic processes of fuel/air mixing, heat release, ignition, local extinction, and combustion have always been a great concern. Great efforts have been focused on the effective mixing and combustion, such as geometric changes, active control, dynamic characteristics and combustion modelling over the scramjet combustors [3,4]. A very recent paper relevant to the current work is from Urzay [2], which reviews the experimental flights and ground-based research programs and highlights associated fundamental flow physics, Large Eddy Simulation (LES) subgrid-scale model development, and its potential full-system numerical simulations in air-breathing propulsion systems for hypersonic flight.

The transverse Jet In Supersonic Crossflow (JISCF) is commonly regarded as efficient ways for mixing and combustion [5,6]. Due to the complex nature of high speed (Mach number > 1) and temperature (~2000K or more) flow inside a very limited space, experimental work [2,7] is expected to be very expensive. Experimental data from the HyShot 2 flight [8,9] and Gamba et al. test rig [10–12] is widely used for numerical benchmark, investigation and further development in recent years [13,14]. Besides, Direct Numerical Simulation (DNS) can be utilised as numerical experiments, such as, Sun & Hu [15], who conduct DNS studies for a transverse air jet in supersonic air crossflow at Mach number of 2.7 under two jet-to-crossflow momentum flux ratios, $J = 1.85$ and 5.5, using a 4th order WENO-CU4 scheme in space and a third-order explicit Runge–Kutta for time advancement. Detailed mean and instantaneous

structures contributing to the mixing process, such as the Counter Rotating Vortex Pair (CRVP), upper Trailing Counter Rotating Vortex Pair (TCRVP), Mach disk formation, etc. are presented. However, for most real-world problems, DNS is also very expensive with the current supercomputing capabilities. This, in return, provides LES a great chance in the fields of JISCF studies, where the work environment is very harsh.

In real JISCF combustion chambers with a ramp, there generally exist complex shock train, bow shock and barrel shock waves, Mach disk, turbulence and boundary layer interactions, combustion with self-ignition due to high-enthalpy and shock aerodynamic heating, local extinction and re-ignition by varies kind of turbulent structures [2,12]. LES of shock-enhanced mixing in a transverse sonic hydrogen JISCF with an inlet 10° compression ramp is conducted at three jet to crossflow momentum flux ratio, J = 0.71, 2.11 & 4.00, by Zhao et. al [16,17], which represents the experimental setup [13]. The bow shock wave and the recirculation zone upstream of the jet orifice contribute to self-ignition and flame anchoring for high J [15,18]. The LES from Zhao et al. [16] also suggests that the CRVP, promoting the mixing process of the fuel jet plume and mainstream air, is significantly affected by the reflected shock wave. The shock-induced baroclinic torque plays an important role on the generation of the vorticity in the near field of the fuel jet, and the place where the reflected shock wave interacts with the jet plume [16,18]. The strong discontinuous of the oblique shock train keep changing the crossflow direction and velocity magnitude, which promotes the mixing process and increases the residence time in the combustor. From the probability density function of the mixture fraction study [16], the coexistence and interaction of the multi-scale structures and combustion undergoing the shock train promote the mixing process of the jet plume and the surrounding air flow.

In order to further improve the mixing and combustion efficiency in JISCF, some researchers focus on pulsed jet frequency [19,20], amplitude [21] and pulsed shape effects [22].

Cutler et al. [19] experimentally investigates the pulsed sonic jet effects on jet penetration in supersonic crossflow. The effective pulsed frequency range is suggested between 10 kHz and 50 kHz. Higher or lower pulsed frequency can lead the pulsed jet flow field to the steady jet mode. The experimental and two-dimensional Unsteady Reynolds Averaged Navier Stokes (URANS) results of Kouchi et al. [20] find that the pulsed jet significantly enhance the jet penetration depth compared with the steady jet. Miller et al. [23] studies the flow structures development with a reaction control jet at St number of 1/6 and 1/3, operating in a Mach 5 laminar boundary layer crossflow using implicit LES. They suggest the partially collapse of shock structures when the square wave pulsed jet is off, which affects the shedding frequency of shear-layer vortices, the formation of longitudinal counter-rotating vortices and the penetration. URANS study of a pulsed jet with different wave shapes namely sine, square and triangle waves, is investigated by Du et al. [22]. In order to achieve adequate fuel/air mixing, LES is employed by Shi et al. [24] to study the influence of pulsed excitation on the flow field and mixing characteristics in transverse JISCF. The results indicate that the pulsed jet excitation has a great influence on the dynamic shock characteristics and large-scale structures in the near-field but little effects in the far-field. DNS is also employed to study the mixing behaviour of square wave pulsed jets in crossflow with several jet to cross flow ratios and pulse conditions, thus the behaviour of vortex rings in crossflow and hairpin vortices behaviour. The proposed regime map help to predict duty cycle, modulation and pulse energy by determining their effect on the equivalent stroke and velocity ratios [25]. Optimization of pulsed jets in crossflow of scramjet is investigated by Randolph et al. [26] in terms of the penetration depth, mixing etc. as injection has to be limited to heights of the combustor core so as to avoid a large thermal loading on the combustor walls. Supersonic crossflow going through the bow shock wave and Mach disk is found to reduce the dynamic pressure of the gaseous injectant to a fraction of its original value and pressure loss [26]. Due to the complexity of the fluid physics,

the expensive experimental and numerical work, the relevant research in this field is still very limited. Zhao et al. [21] perform a 3D pulsed hydrogen JISCF study at $J = 2.11$ using URANS and k-ω SST model to study the frequency and amplitude effects on fuel jet penetration, mixing efficiency, decay rate of the maximum hydrogen mass fraction and total pressure losses. An optimal frequency, 50kHz, is suggested which is within the range proposed by Cutler et al. [19]. It is found that the decay rate of the maximum mass fraction of hydrogen in the farfield downstream is related to the frequency of the pulsed jet. The advantage of the pulsed frequency and amplitude has little effect on the total pressure recovery coefficient [19]. The frontier work in JISCF is to utilise of shock waves to control supersonic mixing and combustion of chemically reacting turbulent flow with a minimum total pressure loss, which motives the current work to investigate the further enhanced mechanism behind the pulsed jet and optimal frequency.

In our previous work [21], the URANS is used to obtain the optimal pulsed jet frequency in a modelled JISCF. The results suggest that the case with pulsed jet frequency of 50 kHz has the optimal mixing performance in the modelled JISCF. However, the enhanced mixing and combustion mechanism with the optimal pulsed jet frequency is still unknown with the URANS simulations. Therefore, in order to uncover the enhanced mechanism of mixing and combustion with the optimal pulsed jet frequency, the LES of the steady (non-pulsed) and optimal pulsed jet frequency of 50 kHz are performed with the $J = 2.11$ based on URANS [21] (pulsed jet frequency effects) studies of transverse hydrogen jet in supersonic air crossflow with a 10$^\text{o}$ ramp at $M = 2.8$. In addition to the flow and flame structures, flame stabilization mechanism and combustion mode, the instabilities and evolutions of the coherent structures and shock waves and their impacts on the fuel mixing and stability of the flame are also assessed with the Power Spectra Density (PSD) and wavelet analysis. This article is organized as follows: in Section 2, simplified description of the physical model is presented. Subsequently, the details

of LES method including the governing equations, numerical and mesh quality aspects with benchmark, boundary conditions are addressed. The current LES results are also assessed with various criteria in Section 2 before detailed discussions of flow and flame structures, flame stabilization, combustion mode, enhanced mixing and combustion mechanism with pulsed jet frequency in Section 3. The main conclusions and suggestions are summarized in Section 4.

2 Physical model and numerical methods

2.1 Physical model

The schematic of the combustion chamber representing the experiment of Gamba et al. [10] and the computational grid are shown in Fig. 1, which is consistent with that employed in LES [17] and URANS [21]. Inlet height of the combustor is 23 mm; the compression ramp has a divergence angle of 10° to generate a shock train. The injection orifice with a diameter of D = 2 mm is located at 70 mm downstream of the supersonic crossflow inlet. The height of constant area section is 15 mm in the normal y-direction with a width of 75 mm in the spanwise z-direction. The Mach number of high-enthalpy air at the inlet of the combustion chamber is 2.8 and the Mach number at the fuel jet is 1. Detailed parameters of the transverse steady JISCF are shown in Table 1. According to previous studies [19–21,24], a sinusoidal pulsed excitation is used for the fuel jet with the jet to crossflow flux ratio remains constant over one cycle, which is expressed as,

$$J = J_0 + J_A sin(2\pi f t), \tag{1}$$

where, J_0 is the jet to cross-flow flux ratio of steady jet, J_A is the amplitude of pulsed jet, and f is the frequency of pulsed jet. In the numerical simulation of this paper, the steady jet to cross-flow flux ration is set as 2.11. As suggested in the previous URANS study [21], for $J_0 = 2.11$ and $J_A = 1$, the optimal pulsed frequency for mixing is 50kHz for the present LES

investigations, and the corresponding Strouhal number ($St = fD/U_{crossflow}$) is about 0.05. The other setups can be found in the relevant sections below.

Table 1 Inflow conditions of the steady hydrogen jet and incoming air stream

	M_a	P_a/kP_a	T_a/K	$Y(H_2)$	$Y(O_2)$	$Y(N_2)$
Hydrogen jet	1.0	668.25	250	1.0	0	0
Air	2.8	40	1200	0	0.232	0.768

2.2 Governing equations

The filtered LES compressible governing equations are

$$\frac{\partial \bar{\rho}}{\partial t} + \frac{\partial \bar{\rho}\tilde{u}_j}{\partial x_j} = 0, \tag{2}$$

$$\frac{\partial \bar{\rho}\tilde{u}_i}{\partial t} + \frac{\partial \bar{\rho}\tilde{u}_i\tilde{u}_j}{\partial x_j} = -\frac{\partial \bar{p}}{\partial x_i} + \frac{\partial}{\partial x_j}\left(\bar{\tau}_{ij} - \tau_{ij}^{sgs}\right), \tag{3}$$

$$\frac{\partial \bar{\rho}\tilde{E}}{\partial t} + \frac{\partial}{\partial x_j}\left[\left(\bar{\rho}\tilde{E} + \bar{p}\right)\tilde{u}_j\right] = \frac{\partial}{\partial x_j}\left[\lambda\frac{\partial \tilde{T}}{\partial x_j} + \tilde{u}_i\bar{\tau}_{ij} - H^{sgs} - \sigma^{sgs}\right] + \overline{\dot{\omega}_T}, \tag{4}$$

$$\frac{\partial \bar{\rho}\tilde{Y}_m}{\partial t} + \frac{\partial \bar{\rho}\tilde{u}_j\tilde{Y}_m}{\partial x_j} = \frac{\partial}{\partial x_j}\left[\bar{\rho}D\frac{\partial \tilde{Y}_m}{\partial x_j} - \tau_{\tilde{Y}_m}^{sgs}\right] + \overline{\dot{\omega}_m} \quad (m = 1,\cdots,N), \tag{5}$$

$$\bar{P} = \bar{\rho}R\left(\tilde{Y}_m\right)\tilde{T}, \tag{6}$$

where, superscript "~" denotes Favre-filtered parameters, and "-" denotes spatially-filtered parameters for LES. $\bar{\rho}$, $\tilde{u}_j$, $\tilde{Y}_m$, $\bar{p}$ and $\tilde{T}$ are filtered density, velocity, mass fraction of species m, pressure and temperature, respectively. $D = \mu/\rho S_c$ in equation (5) is the molecular mass diffusivity, where $\mu = \frac{A_s\sqrt{T}}{1+\frac{T_s}{T}}$ is the dynamic viscosity by using Sutherland's law and S_c is Schmidt number. $\lambda = \mu C_p/Pr$ is the molecular thermal diffusivity, where C_p is the mixture specific heat at constant pressure and the Prandtl number Pr is 0.72. $R\left(\tilde{Y}_m\right)$ is the mixture gas constant. The filtered viscous stress $\bar{\tau}_{ij}$ is defined based on the Eddy viscosity hypothesis as

$$\bar{\tau}_{ij} = \mu \left(2\tilde{S}_{ij} - \frac{2}{3}\mu\tilde{S}_{kk}\delta_{ij} \right), \tag{7}$$

where, $S_{ij} = \frac{1}{2}\left(\frac{\partial u_j}{\partial x_i} + \frac{\partial u_i}{\partial x_j}\right)$ is the strain rate tensor and δ_{ij} is the kronecker operator. The

filtered total sensible energy is

$$\tilde{E} = \tilde{e} + \frac{1}{2}\tilde{u}_j^2 + k^{sgs}, \tag{8}$$

where, $\tilde{e} = \tilde{h}_s - \tilde{P}/\tilde{\rho}$ is internal energy, $\frac{1}{2}\tilde{u}_j^2$ is resolved kinetic energy and k^{sgs} is the sub-

grid kinetic energy. The $\tilde{h}_s$ in the equation of internal energy is sensible enthalpy, expressed as

$$\tilde{h}_s = \sum_{m=1}^{N} \tilde{Y}_m \int_{T_0}^{\tilde{T}} C_{p,m} dT, \tag{9}$$

The reaction source term in the filtered energy equation (4) is

$$\overline{\dot{\omega}_T} = \sum_{m=1}^{N} \overline{\dot{\omega}_m} \Delta h_{f,m}^o. \tag{10}$$

where, $\Delta h_{f,m}^o$ is the formation enthalpy of m-th species. Note that in Eq. (6) the sub-grid

fluctuations of density and temperature are neglected. Different from the energy equation for

low-Mach-number flows, the work done by the shear stress $\tilde{u}_j\bar{\tau}_{ij}$, the sub-grid enthalpy flux

H^{sgs}, the sub-grid scale viscous work σ^{sgs} are included in Eq. (4), which are expected to be

important for fully compressible flows.

All the sub-grid scale terms, denoted by superscript "sgs" in the governing equations (2)

- (5), are closed by the Wall-Adapting Local Eddy-viscosity (WALE) model [27]. The sub-

grid scale term τ_{ij}^{sgs} in Eq. (3) reads

$$\tau_{ij}^{sgs} = \bar{\rho}(\widetilde{u_i u_j} - \tilde{u}_i\tilde{u}_j) = -2\bar{\rho}\mu_t\left(\tilde{s}_{ij} - \frac{1}{3}\tilde{s}_{kk}\delta_{ij}\right) + \frac{2}{3}\bar{\rho}k^{sgs}\delta_{ij}, \tag{11}$$

where the sub-grid kinetic energy and viscosity are modelled by $k^{sgs} = (C_w^2\Delta^2/C_k)^2(\overline{OP})^2$

and $\mu_t = (C_w\Delta)^2\overline{OP}$, in which C_k and C_w are constants and take the values of 0.094 and 0.325

respectively [27]. $\Delta = \sqrt[3]{\Delta_x \Delta_y \Delta_z}$ is the filter width, $\overline{OP} = \dfrac{\left(s_{ij}^d s_{ij}^d\right)^{3/2}}{\left(\tilde{S}_{ij}\tilde{S}_{ij}\right)^{5/2}+\left(s_{ij}^d s_{ij}^d\right)^{5/4}}$ and $S_{ij}^d =$

$\tilde{S}_{ik}\tilde{S}_{kj} + \tilde{\Omega}_{ik}\tilde{\Omega}_{kj} - \frac{1}{3}\delta_{ij}\left[\tilde{S}_{mn}\tilde{S}_{mn} + \tilde{\Omega}_{mn}\tilde{\Omega}_{mn}\right]$, in which $\tilde{\Omega}_{ij}$ is the anti-symmetric part of $\nabla \tilde{u}$.

And $\tau_{ij}^{sgs} = \mu_t(2\tilde{S}_{ij} - \frac{2}{3}\delta_{ij}\tilde{S}_{kk})$. The turbulent Prandtl number is set as $Pr_t = 0.9$. The sub-

grid enthalpy flux H^{sgs} and the sub-grid viscous work σ^{sgs} in Eqs. (4) are closed as

$$H^{sgs} + \sigma^{sgs} = -\frac{\mu_t C_p}{Pr_t}\frac{\partial \tilde{T}}{\partial x_j} - (\mu_t + \mu)\frac{\partial k^{sgs}}{\partial x_j} + \tilde{u}_i \tau_{ij}^{sgs}. \qquad (12)$$

The sub-grid scalar stresses are approximated using an eddy-diffusivity model, which is written

as,

$$\tau_{\tilde{Y}_m}^{sgs} = \bar{\rho}\left(\widetilde{u_i Y_m} - \tilde{u}_i \tilde{Y}_m\right) = -\bar{\rho}\tilde{D}_t \nabla \tilde{Y}_m, \qquad (13)$$

where $\tilde{D}_t$ is the turbulent diffusivity modeled as $\bar{\rho}\tilde{D}_t = \mu_t/Sc_t$, The turbulent Schmidt number

is set as $Sc_t = 0.7$.

The Partially Stirred Reactor (PaSR) model is used to model the interaction between

turbulence and combustion, which has been used to study the turbulent combustion in scramjet

engines [28–31][32]. In the PaSR model, it is assumed that the reacting flow is composed of

reacting fine structures and the surroundings dominated by the large scale structures [33]. The

ratio of the fine reacting structures volume to the LES cell volume κ is modelled as [33]

$$\kappa = \frac{\tau_c}{\tau_c + \tau_*}, \qquad (14)$$

where, $\tau_c = \delta_l/s_l \approx v/s_l^2$ and $\tau_* = \sqrt{\tau_\Delta \tau_k}$ denote the chemical reaction time and subgrid

turbulent mixing time, respectively. Here, δ_l is the laminar flame thickness and s_l is the

laminar flame speed. $\tau_\Delta = \Delta/u_{sgs}$ is the sub-grid time scale and $\tau_k = \left(v/\varepsilon_{sgs}\right)^{1/2}$ is the

Kolmogorov time scale, where $u_{sgs} = \sqrt{2k^{sgs}/3}$ is the sub-grid velocity fluctuation, v is the

laminar kinematic viscosity and $\varepsilon_{sgs} = (u_{sgs})^3/\Delta$ is the sub-grid dissipation rate. A chemical

kinetics model [34] of 9 species (H_2, H, O_2, O, OH, HO_2, H_2O_2, H_2O & N_2) and 19 reaction

steps for hydrogen/air combustion is adopted to describe the combustion process, which has

been validated against the measured ignition delay at elevated pressures [35] and used in Ref.

[32,36] for supersonic combustion simulations. In addition, the predicted ignition delay time,

laminar flame speed and extinction strain rate using the hydrogen/air mechanism are good

agreement with previous experimental data [37–39], which are shown in Fig. 2.

2.3 Numerical Methods

The above filtered LES governing equations are solved using a density-based finite

volume solver, which is constructed under the framework of OpenFOAM [40]. The convective

fluxes are reconstructed using the second-order semi-discrete and non-staggered KNP scheme

[41][42] and the second order central difference Gauss linear scheme is used for the viscous

diffusion. In order to ensure the numerical stability, the van Leer limiter [43] is used for correct

numerical flux calculations with KNP scheme. An explicit modified fourth order Runge-Kutta

scheme with low storage requirement [44] is used for time integration. The CFL number is kept

less than 0.3 to ensure numerical stability, which corresponds the time step on the order of 10^{-9} s. This suggests that the pulsed frequency of 50 kHz will have little effect on the numerics

and statistics in the present simulations. The code development, validation and some relevant

research outcome can be found in [6,17,35,45]. In addition, time-averaging is performed over

six flow through times (6L/U) when a statistical convergence is achieved after four flow

through times (4L/U), where L is the axial length of computational domain and U is the mean

velocity of air inlet.

Dirichlet boundary conditions are used for both the air and hydrogen inlets. The fuel jet inlet velocity profile is prescribed by hyperbolic-tangent function [24,46], and the crossflow inlet mean velocity profile is taken from the three-dimensional RANS simulation. 5% artificial perturbations are added in the inlets. Note that the crossflow inlet is located at 35D upstream of the fuel jet, which means that the turbulent random velocity fluctuations added will have little effect on the flame behaviours with such a long distance. The interactions between the fuel jet and supersonic crossflow are the main focus of this paper and the span-wise boundary is located 17.5D away from the fuel jet orifice, which has little effect on the interactions and the flame evolution. Therefore, a periodic boundary condition is applied in the span-wise boundaries. Moreover, such an approach can decrease the computational cost without refining the mesh in the span-wise boundary. Non-reflective boundary condition is used at the outlet. Isothermal no-slip wall boundary condition is applied for all the walls of the combustor.

Table 2 Detailed information of mesh

Mesh	$N_x \times N_y \times N_z$	Total number	y^+ of up wall	y^+ of down wall
Coarse mesh	401×61×201	4.8 million	2.4 ~ 4.3	1.3 ~ 3.7
Medium mesh	651×121×341	26.5 million	0.8 ~ 2.1	0.5 ~ 1.4
Fine mesh	1001×171×501	85 million	≤ 1	≤ 1

2.4 LES Validation against Experiment and Various Criteria

In the present simulations, three sets of computational mesh, coarse, medium and fine, with 4.8, 26.52 and 85 million hexahedral cells, respectively, are generated for the mesh sensitivity analysis. In order to improve numerical accuracies, in addition to the fuel jet plume region, mesh refinement is performed near the wall and the injection orifice to yield $y^+ \leq 1$ for the first grid adjacent to the wall for the fine mesh (seen in Table 2). The mesh quality in

Δx^+ and Δz^+ directions are improved as well, the ranges of which are 0.4 ~ 4.9 and 0.5 ~ 4.3 respectively.

Figure 3(a) shows the distribution of heat release rate (HRR) and pressure lined-contours (range 20 - 800kPa). A second shock-train, formed by the bow and lambda shock waves around the hydrogen jet orifice, combines with the combustor inlet shock-train to generate complex shock-patterns along the combustor. Fig. 3(b) shows the comparison of the current steady jet predictions and available experimental results of mean pressure distributions on the upper wall of the combustor [10,47]. Very good convergence is shown with the medium and fine mesh LES results, and the results fit in the experiments of Gamba et al. [10,47]. The static pressure increases initially at x/D = -28 due to the oblique shock wave, then decreases at x/D = -13 as the expansion fan formed at the joint of the constant section. At the location of x/D = -4, the pressure increases in the separation bubble region due to the interaction between the reflected shock wave and the upper wall. Note that the instantaneous reflected shock location swings back and forth around x/D = 30 due to the unsteady large scale structures. Therefore, for the mean pressure distribution in Fig. 3(b), the statistically average pressure peak on the up wall is not very obvious at x/D = 30. In order to obtain further high-fidelity results for the analysis of supersonic turbulent mixing and combustion mechanism, the fine mesh is chosen for the investigation to follow. The simulation accuracy is also carefully checked against various LES turbulence criteria, such as the well-established resolution criterion by Pope [48] and effect of sub-grid fluctuations on the filtered chemical reaction source terms [49] and power spectra density (PSD).

In LES, large-scale structures associated with turbulent kinetic energy (TKE) generation are resolved while leaving the small-scale structures associated with dissipation being modelled by a SGS model. According to Pope [48], at least 80% of the total TKE being resolved indicates a well-resolved LES. The well-established resolution criterion is defined as,

$$Me = \frac{k_{sgs}}{k_{RES} + k_{sgs}}, \qquad (15)$$

where k_{sgs} is the sub-grid turbulent kinetic energy and k_{RES} is the resolved turbulent kinetic energy,

$$k_{RES} = \frac{1}{2} \langle \langle \tilde{u}_i^2 \rangle - \langle \tilde{u}_i \rangle^2 \rangle, \qquad (16)$$

where $\langle \cdot \rangle$ represents an ensemble averaging. Fig. 4 provides the distributions of Me, which is computed using the data where hydrogen exists ($Y_{H2} > 0.001$). As seen in Fig. 4, the results show a good coherence with the well-established turbulence resolution criterion, $Me \ll 0.2$, indicating that the current LES solver and mesh quality are capable to predict the characteristic of large and relatively small resolved structures. Therefore, the dominant turbulent structures and fluctuations in the flow field can be well captured.

On the other hand, the sub-grid Damköhler numbers (Da_{sgs}) proposed by Krol et al. [49] are used to assess the effect of sub-grid fluctuations on the filtered chemical reaction source terms, which is defined as

$$Da_{sgs} = \frac{\tau_{sgs}}{\tau_c}, \qquad (17)$$

where, τ_{sgs} is the characteristic time of the smallest resolved structure, determined with

$$\tau_{sgs} = \tau_\Delta = \Delta / u_{sgs}. \qquad (18)$$

τ_c is the characteristic time of the chemistry, which is evaluated as $\tau_c = \delta_l / s_l \approx v / s_l^2$ [33]. If the sub-grid Damköhler numbers are much less than 1, the time scale of the chemical reaction is fully solved and the impact of sub-grid fluctuations on the filtered chemical reaction source terms can be ignored [50,51]. Fig. 5 illustrates the probability density distributions (pdf) of the sub-grid Damköhler number where the instantaneous heat release rate (HRR) is greater than one-thousandth of the maximum HRR for each case with the fine mesh. It is clear to see that

the sub-grid Damköhler numbers of the region where the combustion exists are always less than 0.3, with most regions being less than 0.1.

Furthermore, power spectra density (PSD) provides the turbulence energy spectra, which is widely used to evaluate the quality of an LES result. Fig. 6 shows the PSD of the pressure in the shear layers (x/D = 1, y/D = 2 & z/D = 0) and (x/D = 2, y/D =3 & z/D = 0), and fuel jet plume (x/D = 4, y/D = 2 & z/D = 0). Fig. 6(a-c) corresponds to the energy spectra from the steady jet case. In Fig. 6(d-f), the dominant pulsed frequency of 50 kHz (highlight in red) is detected in the above three specific locations as expected. The PSD in Fig. 6 yields good agreement with the -5/3 law, which indicates that the fine grid is sufficient to predict the characteristics of the inertial subrange [48]. Moreover, it is interesting to notice that the PSD from the pulsed jet in Fig. 6 (d-f) follows the -5/3 law better than those from the steady jet in Fig. 6 (a-c), especially at high frequency (10^6 - 10^7 Hz) which is linked to the resolved small-scale structures in LES. This, in return, indicates that, 1) pulsed jet can further enhance the JISCF mixing; 2) the current LES solver with the fine mesh is strongly believed to be able to capture the larger and relative smaller scale structures to resolve for this case. Note that the -5/3 law might be not always valid in the supersonic flow and combustion due to the compressibility effects and short residence time. However, in the current type of supersonic flow, i.e. transverse jet in supersonic cross-flow, with shock train, mixing and combustion processes, the -5/3 law can be used in as a reference for grid resolution validation of the LES turbulence prediction as suggested in Ref. [52].

The experimental work from Gamba et al. [10] provides the mean pressure measurement at the combustor upper wall, and more data for LES validation will be further convincing to readers. Apart from the general turbulence energy cascade theory from large to small structures naturally, the turbulence structures in SIJCF with a ramp experience abrupt flow distortion within short time, such as shock train, bow shock, barrel shock, Mach disk, flame, turbulence

and boundary layer interactions, self-ignition due to high-enthalpy and shock aerodynamic heating, local extinction and re-ignition [16–18]. From our understandings, those in return increase the level and range of turbulence for LES to capture the dominant phenomena accurately on the same mesh, for such kind of problems.

3 Results and discussion

In this section, the extra enhanced turbulence mixing and combustion mechanisms due to the pulsed JISCF are revealed.

3.1 Instantaneous flow field

Figure 7 provides the distribution of numerical Schlieren $\|\nabla\rho\|$ on the central plane at four typical phases during one pulsed cycle, i.e. $0/4T_0$, $1/4T_0$, $2/4T_0$ and $3/4T_0$, where T_0 is the period of pulsed jet. The typical shock structures marked in the $0/4T_0$ snapshot, denote the bow shock wave (B) on the windward side of the jet, the λ shock (L) formed by the interaction between the bow shock and the boundary layer, the barrel shock (Bs), Mach disk (Md) and reflected shock (Rs) at the junction of the barrel shock and Mach disk. In addition, due to the influence of the inlet compression ramp, a reflected shock train (R) is formed in the combustion chamber. It can be seen that the large-scale structures undergo significant changes in the near and far flow field with the pulsed jet effect. The bow shock and the barrel shock waves are deformed in one cycle of the pulsed jet and the angle of bow shock swings forwards ($1/4T_0$) and backwards ($3/4T_0$) by viewing the post-processed animations. The swing of the bow shock wave strongly peps up the shear layer on the windward side to alternate the shear structures. The largest Mach disk appears at $1/4T_0$ while the Mach disk nearly disappears at $3/4T_0$ due to reduced J, which is consistent with the finding in Randolph et al. [26]. The reduced Mach disk (normal shock) during the cycle indicates a less total static pressure loss. The numbers (1-5) marked in Fig. 7 denote five shear vortex structures and their evolutions. Among them, number

1 and 4 represent large-scale shear layer vortex structures formed by two peak moments ($1/4T_0$ and $3/4T_0$), which maintain a state of large-scale structure near the combustor exit. While the shear layer vortex structures (2, 3, and 5) formed at other two instantaneous phases are relatively smaller. Meanwhile, the shear layer vortex structures undergo violent deformation through the reflected shock train, which again promotes the fuel/air mixing process.

The first four images in Fig. 8(a-d) illustrate the distributions of hydrogen mass fraction in the corresponding four pulsed phases. For comparison, the instantaneous hydrogen mass fraction distribution of the steady jet is also given in Fig. 8(e). Clearly, the large-scale hydrogen jet structures (shown as A, B, C in Fig. 8) periodically appears in the downstream due to the pulsed jet, which results in higher jet penetration and much more flow entrainment. The first large scale hydrogen jet structure (A in Fig. 8(a)) is periodically generated at $0/4T_0$. As the size of the barrel shock increases during the course, a large-scale structure is formed at $1/4T_0$ and accompanied by the shear layer structures of the original steady jet. These enlarged shear layer structures are partially distorted by the reflected shock train. Compared with the steady jet, the pulsed jet changes the rotation direction of the large-scale shear layer vortex structures. For pulsed jet shown in Fig. 8(a-d), there are clockwise and counter-clockwise rotating shear layer vortex structures identified by "A". But for the steady jet in Fig. 8(e), only counter-clockwise rotating shear layer vortex structure is found. Changing the rotation direction and going through the reflected shock train, the enlarged vortex structures make perfect mixing, which is conducive to the combustion of the mixture. With these large-scale hydrogen jet structures in pulsed jet, the mixing in the supersonic combustor will be significantly enhanced, and therefore improving the combustion efficiency.

3.2 Flame structures

For the pulsed JISCF, the distribution of heat release rate (HRR) and pressure contour at $0/4T_0$ are plotted in Fig. 9(a). Note that the flow structure does not change much within a period at different phases, therefore only the results at $0/4T_0$ are shown here. It is obvious that the combustion after the bow shock wave has a very intense heat release and is mainly dominated by high-temperature self-ignition. Local flame quenching can be observed in the downstream windward side shear layer, which is mainly due to mixing-limited combustion processes. When the shear layer undergoes aerodynamic heating of the reflected shock waves, the reaction HRR is significantly improved and the combustion flame in the shear layer exists in the form of a thin reaction zone. The large scales (such as "B" marked in Fig. 8) induced by pulsed jet entrain more combustible mixture to interact with the reflected shock. After the interaction between the reflected shock wave and the boundary layer of the low wall, the HRR is also enhanced. On the other hand, the shock wave plays an important role in the flame anchoring and stabilization, and the pressure distribution after the reflected shock is more disordered to strengthen the mixing process.

The distributions of temperature, OH and H_2O mass fraction on the central plane ($z/D=0$) at $0/4T_0$ are also shown in Fig. 9. The temperature after the bow shock location is as high as 2000K or more due to the interaction between the sonic jet and the high enthalpy supersonic compression on the windward side, where auto-ignition occurs. And local flame quenching is observed just downstream of the fuel jet limited by the temperature and supersonic mixing. Reaction after the region between the reflected shock wave and the fuel jet is very intense, resulting in more combustion product of H_2O. In addition to the shock train, the flame is significantly affected by large-scale structures in the pulsed JISCF case.

3.3 Combustion mode analysis

The numerical simulation results suggest that the ignition process has two main aspects: one is the high temperature auto-ignition process and the other is the ignition process caused by the shock compression effects. High temperature auto-ignition mainly occurs in the recirculation zone and the windward shear layer of near field. The results of Boivin et al. [53] suggest that HO_2 can be used as a marker for the auto-ignition process in hydrogen chemical reactions, i.e. the large enough concentration of HO_2 and high reactivity. Fig. 10 shows the distribution of HO_2 on the central plane (z/D=0) at different times of the pulsed jet. It can be found that there is a large amount of HO_2 in the recirculation zone and inside the near-field jet shear layer. Since the supersonic crossflow is high enthalpy and high temperature air, it is easy to have a high temperature auto-ignition in the recirculation zone and the jet shear layer.

As seen in Fig. 9, the ignition is caused by the shock compression. The coupling between the shock compression and the HRR is strong, which in turn causes the ignition of the shear layer after the shock wave. During the process, the core region of the jet plume is also ignited after the reflected shock and a strong flame also occurs near the shock/boundary layer interaction zone, thus a large amount of HO_2 generated after the interaction between the shock wave and fuel jet plume (seen in Fig. 10). In order to further study the relationship between shock wave and HRR, an index is introduced [36],

$$N = \nabla p \cdot \nabla HRR \cdot \|HRR\| / \|HRR\|_{max} \qquad (19)$$

where, $\|HRR\|/\|HRR\|_{max}$ is used to figure out the regions of negligible heat release. Fig. 11 shows the numerical schlieren results and logarithmic distributions of the index N in the central plane (z/D=0). The larger value of N indicates the stronger interactions between the shock wave and the flame. The value of N behind the bow shock wave and upstream of the jet exit, and the reflected shock wave downstream is relatively larger, indicating a strong coupling with the combustion. Local quenching is observed in the shear layer on the windward side and the flame

occurs again behind the reflected shock wave (see Fig. 9a) with large N (See Fig. 11a), which suggests that the ignition process is caused by the shock compression effects. In addition, it is worth noting that the index N in the recirculation zone upstream of the jet orifice also has relatively larger values. This is mainly related to the adverse pressure gradient caused by the supersonic flow encountering the sonic fuel jet upstream of the jet orifice, which in turn forms the low-velocity recirculation zone and contributes to the flame stabilization.

Figure 12 shows the scatter distribution of the OH mass fraction coloured by the flame index (TFI $= (\nabla Y_F \cdot \nabla Y_O)/(|\nabla Y_F||\nabla Y_O|)$) [54] in the mixture fraction space on the central plane at $0/4T_0$, where TFI greater than zero indicating a premixed flame zone, and a value less than 0 being a non-premixed flame zone. The combustion mode of the flame can be identified by combination of flame index and OH mass fraction. Clearly, the region with higher OH is basically a non-premixed flame, and the HRR is mainly based on non-premixed combustion. And there is also a premixed combustion region, which is mainly distributed in the fuel rich region inside the fuel jet shear layer. Note that the scatter distributions of the OH mass fraction in the mixture fraction space within a period at different phases have similar combustion mode as shown in Fig. 12, therefore only the results at $0/4T_0$ are shown here.

To further illustrate, Figure 13 shows the pdf of TFI and the conditional average HRR on TFI at the four typical phases to quantitatively study the combustion HRR mechanism in the pulsed SJICF, where the HRR is not less than one thousandth of the maximum HRR. Results tell that the combustion are mainly dominated by premixed (TFI = 1) and diffusion (TFI = -1) combustion. The HRR is always dominated by the non-premixed combustion, which is significantly changed by the pulsed jet at different phases. It can be concluded from the Fig. 13(b-c) that the higher instantaneous jet flux ratio can increase the HRR of the non-premixed combustion. Due to the delay effect of the pulsed jet, the near-field combustion mode is firstly

affected by the pulsed jet, further indicating the JISCF combustion in the near field is dominated by non-premixed combustion.

3.4 Frequency analysis of instability

Relatively few studies on the unstable frequencies in JISCF have been concerned. The research on the characteristic frequency is mainly focused on the bow shock, barrel shock and out moving shock waves [24]. The characteristic frequency of these shock waves is different from that in the jet shear layer. Therefore, based on the LES results, the characteristic frequency analysis is performed at specific positions in the jet shear layer to understand the instabilities and evolutions of the coherent structures and their impacts on the fuel mixing and stability of the flame.

In this section, Fourier transform of the flow field time signal sequences f(t) is to quantitatively identify these unsteady frequencies, and then the wavelet analysis is used to further confirm these instabilities. From the Fourier transform of the flow field time signal sequences f(t), the PSD as a function of frequency at points and the characteristic frequencies can be obtained [55]. In the Wavelet analysis, an inner products are used to measure the similarity between a signal (f(t)) and an analyzing function (wavelet ψ(t)) [56]. Comparing f(t) to ψ(t) at various scales and positions leads to the two-dimensional representation of f(t). It should be noted that the main difference between the Fourier transform and the wavelet analysis is that wavelets are localized in both time and frequency whereas the standard Fourier transform is only localized in frequency.

Figure 14 shows the density distribution of the steady jet and the spatial positions for the characteristic frequency analysis, labelled as P1-P6. P1 and P2 represent two locations of bow shock, P3 and P4 correspond the barrel shock locations, and P5 and P6 are in the jet shear layer.

Note that Fig. 14 shows the results of steady jet, the corresponding positions of the shock wave and the large-scale structure in the pulsed jet are utterly unchanged or are swung around the detection points at a certain frequency [24].

Figure 15 is the PSD variation against Strouhal number (St) for the steady JISCF case. It can be seen that the St number of bow shock wave is 0.04 at the peak PSD of 2.25, which corresponds to the characteristic frequency of 40 kHz. The barrel shock and the shear layer have the same St-number, both of which are 0.27, and the corresponding dominant characteristic frequency is 270 kHz, which is also called the generation frequency of the shear layer vortex [57]. The equivalent PSD results of pulsed JISCF are shown in Fig. 16. The main St-number of all detection locations is found to be 0.05, and the corresponding dominant characteristic frequency was 50 kHz. This is consistent with the optimal jet pulsed frequency in the LES numerical simulation, which indicates that the unsteady evolution of large-scale structure is dominated by the jet pulsed frequency in the SJICF. In addition, the characteristic frequency corresponding to the evolution of the shear layer vortex is also observed to be 270 kHz (St = 0.27) in the positions of pulsed jet shear layer. From the PSD of the pressure of the steady jet (see Fig. 15) and the pulsed jet (see Fig. 16), it can be seen that the frequency of the pulsed jet is the dominant frequency which affects the evolution of shock waves such as the bow shock and barrel shock and the dynamics of large-scale structures such as the jet shear layers, which is similarly to the results of low-speed pulsed jet in crossflow [58][59].

In order to further determine the characteristic frequencies, especially the low-frequency characteristics of the large-scale evolution, wavelet analysis is carried out with the simultaneous pressure frequency changes with time at the detection points. Figures 17 and 18 are pressure signal wavelet spectra of the steady and pulsed jet, respectively, corresponding to the detection points in Fig. 14. The St-number of bow shock wave captured by the wavelet analysis in the steady jet is 0.4 as seen in Fig. 17 (P1 and P2), and the spectral intensity does

not change with time. In addition, the wavelet spectrum captures a lower characteristic frequency with a St-number of approximately 0.016, which was not observed in the PSD analysis. The wavelet spectrum of pulsed jet as seen in Fig. 18 (P1 and P2) also captures the frequency obtained by the PSD analysis, and the frequency does not change with time. At the same time, a lower characteristic frequency is also observed in the pulsed jet, which is consistent with the steady jet as St $\approx$ 0.016. The characteristic frequencies not captured in the PSD analysis may be related to the expansion wave. In the wavelets of the detection points (P3 and P4) near the windward side of barrel shock wave, two spectra can be observed in the steady jet as seen in Fig. 17, i.e. one is the low St number that does not change with time, and the other is spectrum with high St around 0.27 varying with time. In the pulsed jet as seen in Fig. 18, only the characteristic frequency with a St-number of about 0.05 is observed. In addition, the lower frequency characteristics are not captured in the wavelet spectrum of the detection point near the barrel shock, and the results are consistent with the results of PSD analysis. In the wavelet spectrum of the detection points (P5 and P6) in the shear layer, three characteristic frequencies are observed in the steady jet. The first one is that the spectral intensity does not change with time, and the St-number is about 0.04. The second one is the spectrum with high St-number around 0.27 varying in time, indicating that the vortex shedding of the shear layer irregularity. The third one is the same as the position of the bow shock wave, for which the lower St-number is also about 0.016. In Fig. 18, in addition to the pulsed dominant characteristic frequency St = 0.05, the characteristic frequency St $\approx$ 0.27 of the unsteady shear layer vortex is captured, which is consistent with the result in the PSD analysis. The lower characteristic frequency is also captured at the detection point P5, for which the St-number is about 0.016.

3.5 Effect of pulsed frequency on mixing and combustion efficiency

From the above analysis, it can be found that the optimal pulsed frequency for the mixing and combustion efficiency, i.e. 50 kHz, is very close to the characteristic frequency of bow shock wave (about 40 kHz as shown in Fig. 15). There may be some inherent relationship between the optimal pulsed jet frequency with the frequency of bow shock. In order to verify this hypothesis, an additional case with pulsed frequency of 40 kHz should be performed. However, in order to reduce the computational cost, here the URANS following our previous work [21] is used. Note that the study in Ref. [21] is non-reacting case, here the URANS simulation with the similar combustion model in the present LES simulation is employed. The mixing efficiency and combustion efficiency are used to evaluate the effect of pulsed jet frequency. The mixing efficiency is defined as the ratio of the effective mass flow rate of burnable hydrogen to total hydrogen mass flow rate, which can also be found in our previous work [21]. Following Kumaran and Babu [1], the combustion efficiency is defined as the ratio of the amount of fuel that is consumed completely to the total amount of fuel injected, which reads,

$$
\eta_c = \frac{\int_S \frac{1}{9} \langle \tilde{Y}_{H2O} \rangle \langle \bar{\rho} \rangle \langle \tilde{u}_n \rangle dA}{\int_S \langle \tilde{Y}_{H2} \rangle \langle \bar{\rho} \rangle \langle \tilde{u}_n \rangle dA}, \tag{20}
$$

where, $\langle \tilde{Y}_{H2O} \rangle$ is the mass fraction of consumed hydrogen and $\langle \tilde{Y}_{H2} \rangle$ is the time averaged mass fraction of hydrogen. $\langle \bar{\rho} \rangle \langle \tilde{u}_n \rangle dA$ represents the fluid mass flow rate at a given cross section along x-direction and S is the area of the considered cross section.

Fig. 19 shows the mixing efficiency and combustion efficiency from the URANS simulations. The results in terms of mixing and combustion efficiency, and jet penetration are compared with Zhao et al. [21] and suggest that the pulsed frequency of 40 kHz (not 50 kHz) is the best for improving the current mixing and combustion efficiency. In other word, setting

24

the pulsed frequency the same as the bow shock characteristic frequency, extra mixing and combustion efficiency, and jet penetration can be achieved.

Conclusion

Large eddy simulation of a pulsed jet combustion in supersonic crossflow has been performed to study the supersonic combustion and the mechanism of enhanced mixing and combustion for the optimal pulsed frequency, i.e. 50 KHz. For comparison and validation, a corresponding steady jet in supersonic crossflow has been carried out. Three levels of grid refinement are used to assess the mesh sensitivity analysis. The numerical method and mesh resolution are validated by comparison with the experimental data and by further analysing various resolution criteria with the fine mesh.

As the pulsed jet issuing into supersonic crossflow, the swing bow shock wave interacts strongly with the jet shear layer and barrel shock wave to intensify the jet penetration depth. The energetic structures from the barrel shock and shear vortex ('C' structure evolution in Fig. 7) are further enlarged at the phase of $1/4T_0$ periodically due to the swing forward and backward effect. There coexists clockwise and counter-clockwise rotating shear layer vortex structures in the pulsed jet, while only counter-clockwise rotating shear layer vortex structure is found in the steady case. For the JISCF with a ramp, the optimal pulsed jet promotes the mixing and combustion processes with a wider range of turbulence structures and energy spectra be captured. The reflected shock waves have strong coupling effects with the HRR, especially the significant increasing of HRR due to the aerodynamic heating after the shock wave. In the pulsed jet case, the HRR is dominated by the non-premixed combustion, and the pulsed jet is found to have little effect on the premixed combustion heat release. The pulsed jet is also found to improve the non-premixed dominant heat release rate, but not the premixed one.

The instabilities and evolutions of the coherent structures and shock waves and their impacts on the fuel mixing and stability of the flame are further studied by using the PSD and wavelet analysis. It is worth noting that the pulsed jet frequency has strong coupling effects with the bow shock swing back and forward frequency, the jet shear layer and barrel shock frequencies (i.e. 50 kHz), while the corresponding characteristic frequencies are 40, 270 and 270 kHz, respectively, for the steady jet case. Furthermore, setting the pulsed jet frequency to 40 kHz, the bow shock characteristic frequency found in the steady case, the mixing and combustion efficiency can be further improved by using URANS simulations. This suggests that the mechanism of enhanced mixing and combustion efficiency relevant to the optimal frequency may be related to the bow shock swing back and forward frequency (i.e. 40 kHz, not 50 kHz in the present modelled SJICF), which could provide us guidelines to further investigate the relationship between the active control frequency and the bow shock characteristic frequency numerically or experimentally to possibly generate empirical formulae for a specific pulsed JISCF application.

Acknowledgement

Reference

[1]   E.T. Curran, Scramjet engines: the first forty years, J. Propuls. Power. 17 (2001) 1138–1148.

[2]   J. Urzay, Supersonic combustion in air-breathing propulsion systems for hypersonic flight, Annu. Rev. Fluid Mech. 50 (2018) 593–627.

[3]   W. Huang, Mixing enhancement strategies and their mechanisms in supersonic flows: a brief review, Acta Astronaut. 145 (2018) 492–500.

[4]   E.D. Gonzalez-Juez, A.R. Kerstein, R. Ranjan, S. Menon, Advances and challenges in modeling high-speed turbulent combustion in propulsion systems, Prog. Energy Combust. Sci. 60 (2017) 26–67.

[5]   A.R. Karagozian, Transverse jets and their control, Prog. Energy Combust. Sci. 36 (2010) 531–553.

[6]   M. Zhao, Y. Bian, Q. Li, T. Ye, Large eddy simulation of transverse single/double jet in supersonic crossflow, Aerosp. Sci. Technol. 89 (2019) 31–45.

[7]   A. Ben-Yakar, Experimental investigation of mixing and ignition of transverse jets in supersonic crossflows, 2000.

[8]   M.K. Smart, N.E. Hass, A. Paull, Flight data analysis of the HyShot 2 scramjet flight experiment, AIAA J. 44 (2006) 2366–2375.

[9]   N. Hass, M. Smart, A. Paull, Flight Data Analysis of the HYSHOT 2, in: AIAA/CIRA 13th Int. Sp. Planes Hypersonics Syst. Technol. Conf., 2005: pp. 3354.

[10]   M. Gamba, V. Miller, M.G. Mungal, R. Hanson, Ignition and flame structure in a compact inlet/scramjet combustor model, in: 17th AIAA Int. Sp. Planes Hypersonic Syst. Technol. Conf., 2011: pp. 2366.

[11]   M. Gamba, M.G. Mungal, R. Hanson, Ignition and near-wall burning in transverse hydrogen jets in supersonic crossflow, in: 49th AIAA Aerosp. Sci. Meet. Incl. New Horizons Forum Aerosp. Expo., 2011: pp. 319.

[12]   M. Gamba, M.G. Mungal, Ignition, flame structure and near-wall burning in transverse hydrogen jets in supersonic crossflow, J. Fluid Mech. 780 (2015) 226–273.

[13] S.J. Laurence, D. Lieber, J.M. Schramm, K. Hannemann, J. Larsson, Incipient thermal choking and stable shock-train formation in the heat-release region of a scramjet combustor. Part I: Shock-tunnel experiments, Combust. Flame. 162 (2015) 921–931.

[14] K. Nordin-Bates, C. Fureby, S. Karl, K. Hannemann, Understanding scramjet combustion using LES of the HyShot II combustor, Proc. Combust. Inst. 36 (2017) 2893–2900.

[15] M.-B. Sun, Z.W. Hu, Generation of upper trailing counter-rotating vortices of a sonic jet in a supersonic crossflow, AIAA J. 56 (2018) 1047–1059.

[16] M. Zhao, Q. Li, T. Ye, Investigation of the mixing characteristics in a transverse hydrogen injection combustor with an inlet compression ramp, Acta Astronaut. 160 (2019) 479–488.

[17] M. Zhao, T. Ye, C. Cao, T. Zhou, M. Zhu, Study of sonic injection from circular injector into a supersonic cross-flow using large eddy simulation, Int. J. Hydrogen Energy. 41 (2016) 17657-17669.

[18] M. Zhao, T. Zhou, T. Ye, M. Zhu, H. Zhang, Large eddy simulation of reacting flow in a hydrogen jet into supersonic cross-flow combustor with an inlet compression ramp, Int. J. Hydrogen Energy. 42 (2017) 16782-16792.

[19] A. Cutler, G. Harding, G. Diskin, High frequency supersonic pulsed injection, in: 39th Aerosp. Sci. Meet. Exhib., 2001: pp. 517.

[20] T. Kouchi, K. Sasaya, J. Watanabe, H. Shibayama, G. Masuya, Penetration characteristics of pulsed injection into supersonic crossflow, in: 46th AIAA/ASME/SAE/ASEE Jt. Propuls. Conf. Exhib., 2010: pp. 6645.

[21] M. Zhao, T. Ye, URANS study of pulsed hydrogen jet characteristics and mixing enhancement in supersonic crossflow, Int. J. Hydrogen Energy. 44 (2019) 20493–20503.

[22] Z. Du, W. Huang, L. Yan, L. Li, Z. Chen, S. Li, RANS study of steady and pulsed gaseous jets into a supersonic crossflow, Int. J. Heat Mass Transf. 136 (2019) 157–169.

[23] W.A. Miller, P.R. Medwell, C.J. Doolan, M. Kim, Numerical investigation of a pulsed reaction control jet in hypersonic crossflow, Phys. Fluids. 30 (2018) 106108.

[24] H. Shi, G. Wang, X. Luo, J. Yang, X.-Y. Lu, Large-eddy simulation of a pulsed jet into a supersonic crossflow, Comput. Fluids. 140 (2016) 320–333.

[25] R. Sau, K. Mahesh, Optimization of pulsed jets in crossflow, J. Fluid Mech. 653 (2010) 365–390.

[26] H. Randolph, L. Chew, H. Johari, Pulsed jets in supersonic crossflow, J. Propuls. Power. 10 (1994) 746–748.

[27] F. Nicoud, F. Ducros, Subgrid-Scale Stress Modelling Based on the Square of the Velocity Gradient Tensor, 62 (1999) 183–200.

[28] C. Fureby, M. Chapuis, E. Fedina, S. Karl, CFD analysis of the HyShot II scramjet combustor, Proc. Combust. Inst. 33 (2011) 2399–2405.

[29] M. Chapuis, E. Fedina, C. Fureby, K. Hannemann, S. Karl, J.M. Schramm, A computational study of the HyShot II combustor performance, Proc. Combust. Inst. 34 (2013) 2101–2109.

[30] M. Berglund, C. Fureby, LES of supersonic combustion in a scramjet engine model, Proc. Combust. Inst. 31 (2007) 2497–2504.

[31] M. Berglund, E. Fedina, C. Fureby, J. Tegnér, V. Sabel'nikov, Finite Rate Chemistry Large-Eddy Simulation of Self-Ignition in Supersonic Combustion Ramjet, AIAA J. 48 (2010) 540–550.

[32] C. Fureby, A Comparative Study of Subgrid Models, Reaction Mechanisms and Combustion Models in LES of Supersonic Combustion, in: AIAA Propuls. Energy 2019 Forum, 2019: pp. 4273.

[33] V. Sabelnikov, C. Fureby, LES combustion modeling for high Re flames using a multi-phase analogy, Combust. Flame. 160 (2013) 83–96.

[34] C.J. Jachimowski, An analytical study of the hydrogen-air reaction mechanism with application to scramjet combustion, 1988.

[35] M. Zhao, J.-M. Li, C.J. Teo, B.C. Khoo, H. Zhang, Effects of variable total pressures on instability and extinction of rotating detonation combustion, Flow, Turbul. Combust. 104 (2020) 261-290.

[36] Y. Moule, V. Sabelnikov, A. Mura, Highly resolved numerical simulation of combustion in supersonic hydrogen–air coflowing jets, Combust. Flame. 161 (2014) 2647–2668.

[37] M. Slack, A. Grillo, Investigation of hydrogen-air ignition sensitized by nitric oxide and by nitrogen dioxide, 1977.

[38] O.C. Kwon, G.M. Faeth, Flame/stretch interactions of premixed hydrogen-fueled flames: measurements and predictions, Combust. Flame. 124 (2001) 590–610.

[39] M. Juniper, N. Darabiha, S. Candel, The extinction limits of a hydrogen counterflow diffusion flame above liquid oxygen, Combust. Flame. 135 (2003) 87–96.

[40] H. Jasak, A. Jemcov, Z. Tukovic, OpenFOAM: A C++ library for complex physics simulations, in: Int. Work. Coupled Methods Numer. Dyn., IUC Dubrovnik Croatia, 2007: pp. 1–20.

[41] C.J. Greenshields, H.G. Weller, L. Gasparini, J.M. Reese, Implementation of semi-discrete, non-staggered central schemes in a colocated, polyhedral, finite volume framework, for high-speed viscous flows, Int. J. Numer. Methods Fluids. 63 (2010) 1–21.

[42] A. Kurganov, E. Tadmor, New High-Resolution Central Schemes for Nonlinear Conservation Laws and Convection-Diffusion Equations, J. Comput. Phys. 160 (2000) 241–282.

[43] B. van Leer, Towards the ultimate conservative difference scheme. II. Monotonicity and conservation combined in a second-order scheme, J. Comput. Phys. 14 (1974) 361–370.

[44] K.A. Hoffmann, S.T. Chiang, Computational fluid dynamics volume I, Eng. Educ. Syst. 2000.

[45] Y. Bian, M. Zhao, Q. Li, T. Ye, Characteristics and mixing enhancement of a self-throttling system in a supersonic flow with transverse injections, Int. J. Hydrogen Energy. 43 (2018) 13550–13562.

[46] G. Wang, L. Chen, X. Lu, Effects of the injector geometry on a sonic jet into a supersonic crossflow, Sci. China Physics, Mech. Astron. 56 (2013) 366–377.

[47] M. Gamba, V. Miller, G. Mungal, R. Hanson, Combustion characteristics of an inlet/supersonic combustor model, in: 50th AIAA Aerosp. Sci. Meet. Incl. New Horizons Forum Aerosp. Expo., 2012: pp. 612.

[48] S.B. Pope, Turbulent flows, 2001.

[49] M.C. Krol, M.J. Molemaker, J.V.G. de Arellano, Effects of turbulence and heterogeneous emissions on photochemically active species in the convective boundary layer, J. Geophys. Res. Atmos. 105 (2000) 6871–6884.

[50] C. Duwig, K.-J. Nogenmyr, C. Chan, M.J. Dunn, Large eddy simulations of a piloted lean premix jet flame using finite-rate chemistry, Combust. Theory Model. 15 (2011) 537–568.

[51] L. Bouheraoua, P. Domingo, G. Ribert, Large-eddy simulation of a supersonic lifted jet flame: analysis of the turbulent flame base, Combust. Flame. 179 (2017) 199–218.

[52] S. Kawai, S.K. Lele, Large-eddy simulation of jet mixing in supersonic crossflows, AIAA J. 48 (2010) 2063–2083.

[53] P. Boivin, A. Dauptain, C. Jiménez, B. Cuenot, Simulation of a supersonic hydrogen–air autoignition-stabilized flame using reduced chemistry, Combust. Flame. 159 (2012) 1779–1790.

[54] H. Yamashita, M. Shimada, T. Takeno, A numerical study on flame stability at the transition point of jet diffusion flames, in: Symp. Combust., Elsevier, 1996: pp. 27–34.

[55] P. Welch, The use of fast Fourier transform for the estimation of power spectra: a method based on time averaging over short, modified periodograms, IEEE Trans. Audio Electroacoust. 15 (1967) 70–73.

[56] D.A. Lysenko, I.S. Ertesvåg, K.E. Rian, Large-eddy simulation of the flow over a circular cylinder at Reynolds number 2×10^{4}, Flow, Turbul. Combust. 92 (2014) 673–698.

[57] A. Ben-Yakar, M.G. Mungal, R.K. Hanson, Time evolution and mixing characteristics of hydrogen and ethylene transverse jets in supersonic crossflows, Phys. Fluids. 18 (2006) 26101.

[58] J. Davitian, D. Getsinger, C. Hendrickson, A.R. Karagozian, Transition to global instability in transverse-jet shear layers, J. Fluid Mech. 661 (2010) 294–315.

[59] J. Davitian, C. Hendrickson, D. Getsinger, R.T. M'closkey, A.R. Karagozian, Strategic control of transverse jet shear layer instabilities, AIAA J. 48 (2010) 2145–2156.
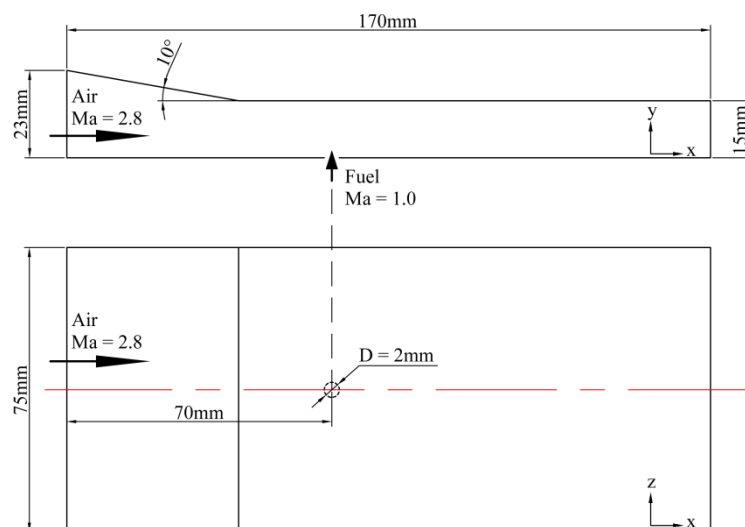
(a) Schematic diagram of the physical model and computational domain
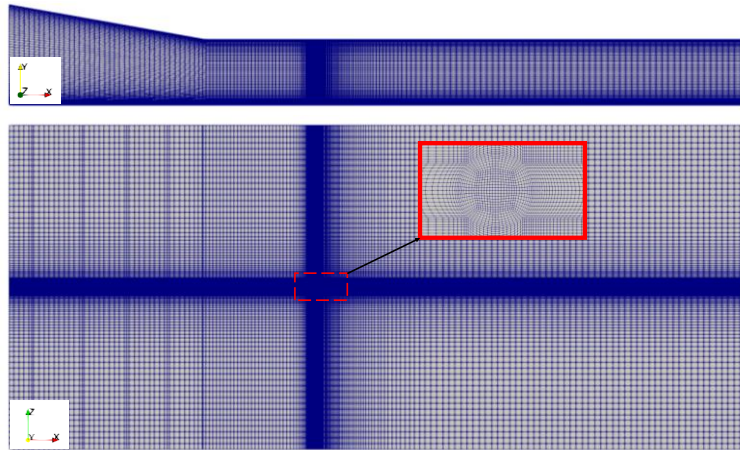
(b) Schematic of the grid in the central plane, normal y-direction plane

Fig. 1 Schematic diagram of the physical model and computational grid [21].
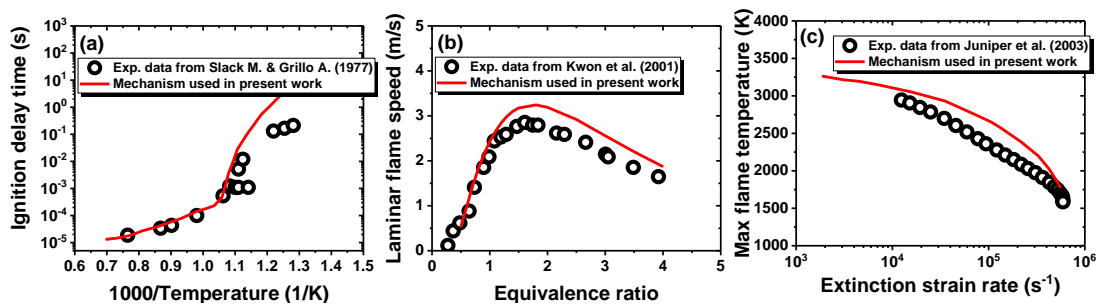
Fig. 2 Comparison of (a) ignition delay time, (b) laminar flame speed and (c) extinction strain rate at 1 atm for H2-air mixtures with experimental data [37–39].

(a)

(b)
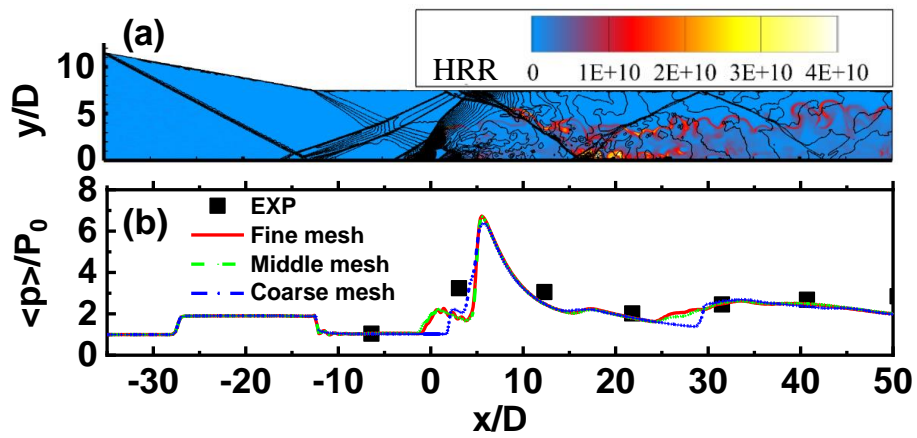
Fig. 3 Numerical convergence and experimental validation for the steady jet: (a) distribution of HRR (J/m3/s) and pressure lined-contours (20~800kPa); (b) Upper wall mean pressure distribution between LESs and experiments [10,47] in the central plane (z/D = 0).
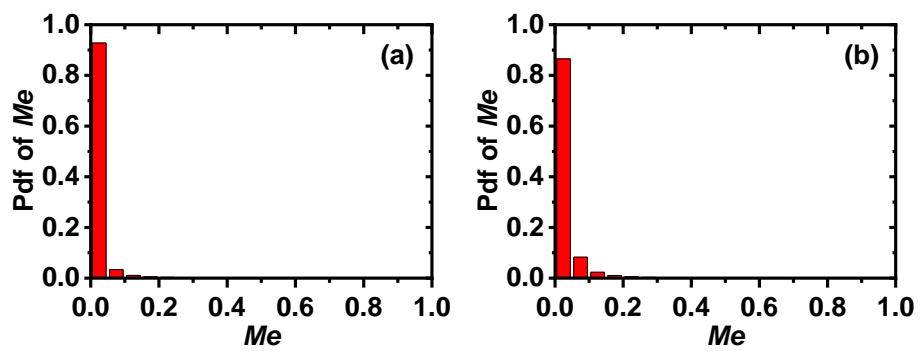
Fig. 4 Pdf of *Me* for the cases with: (a) steady jet and (b) pulsed jet.
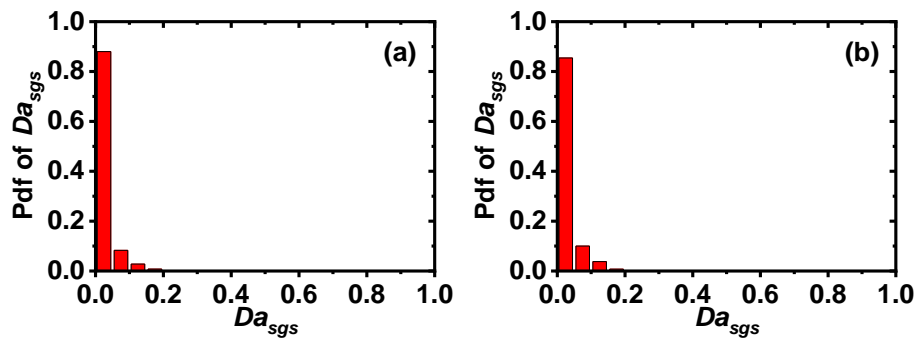
Fig. 5 Pdf of the Da_{sgs} for the cases with (a) steady jet and (b) pulsed jet.
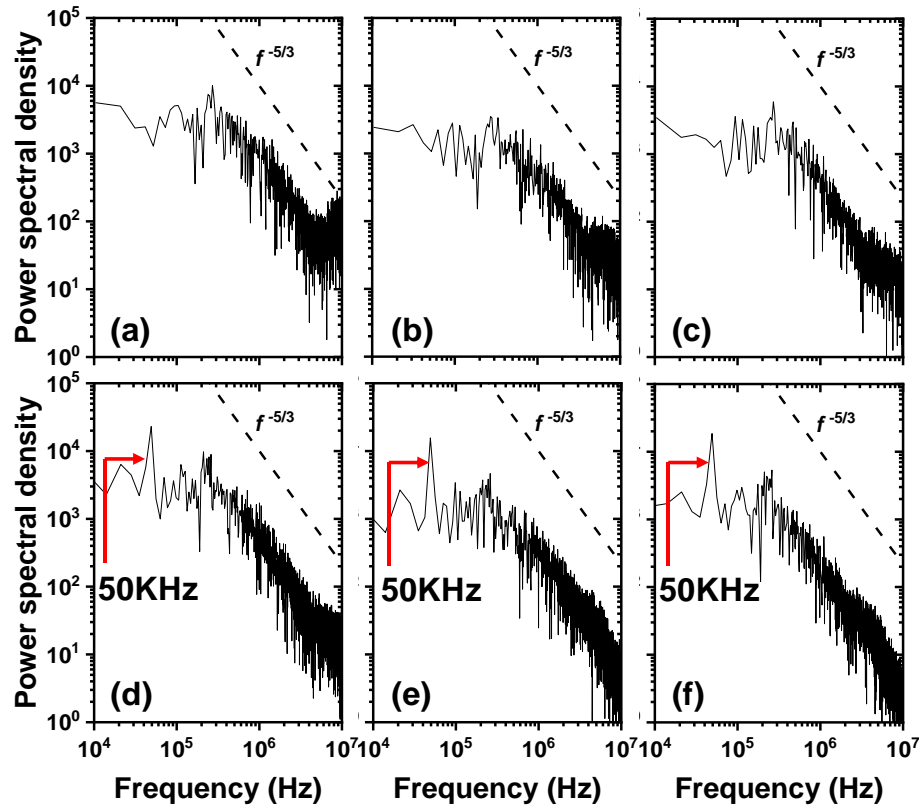
Fig. 6 PSD of the pressure for (a-c) steady jet and (d-f) pulsed jet: (a, d) in the shear layer (x/D = 1, y/D = 2 & z/D = 0) and (b, e) (x/D = 2, y/D =3 & z/D = 0) and (c, f) in the fuel jet plume (x/D = 4, y/D = 2 & z/D = 0).
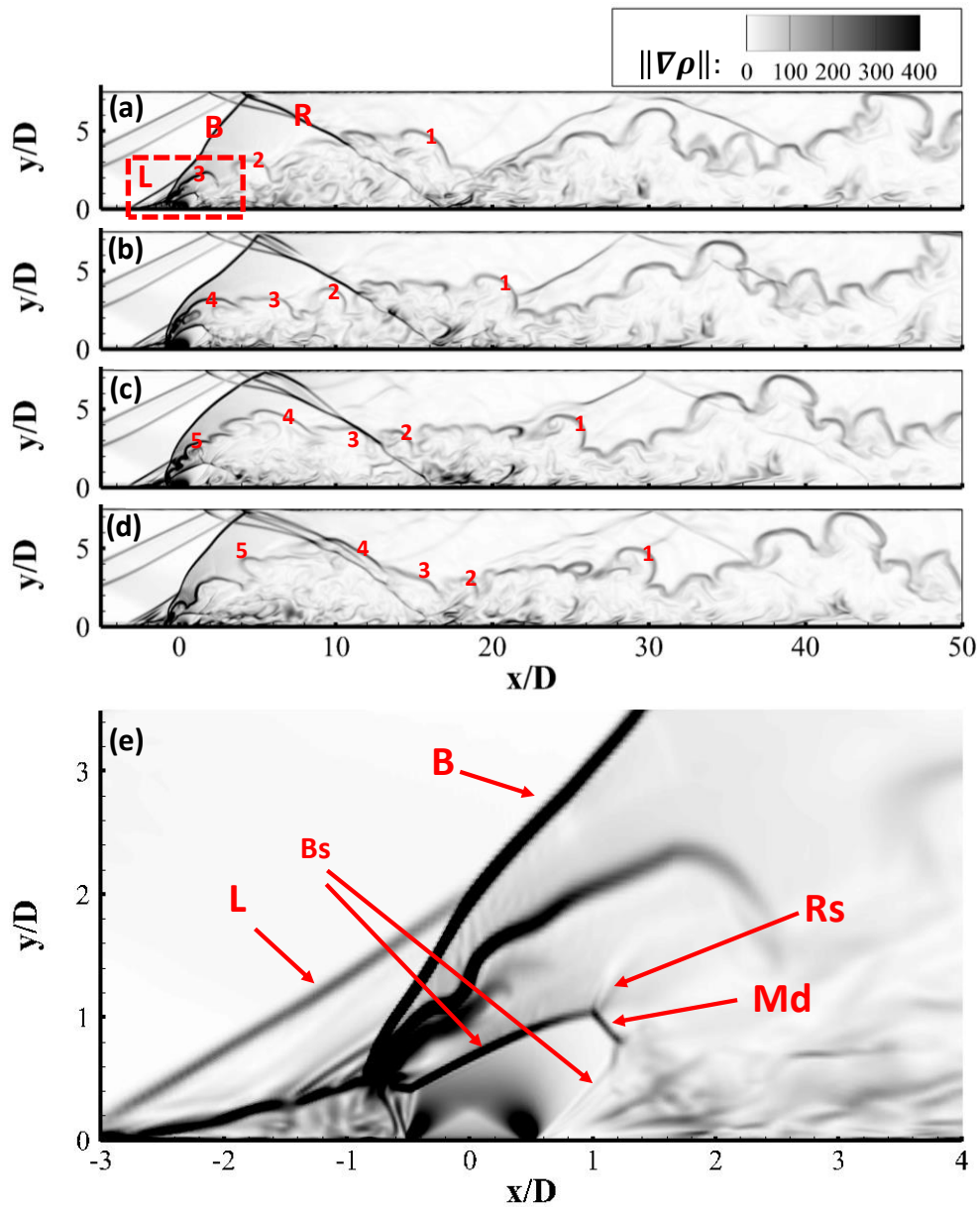
Fig. 7 Distributions of numerical Schlieren $\|\nabla\rho\|$ in the central plane ($z/D = 0$) at four typical phases during one pulsed cycle, (a) $0/4T_0$, (b) $1/4T_0$, (c) $2/4T_0$, (d) $3/4T_0$, and (e) zoom view close to the injector
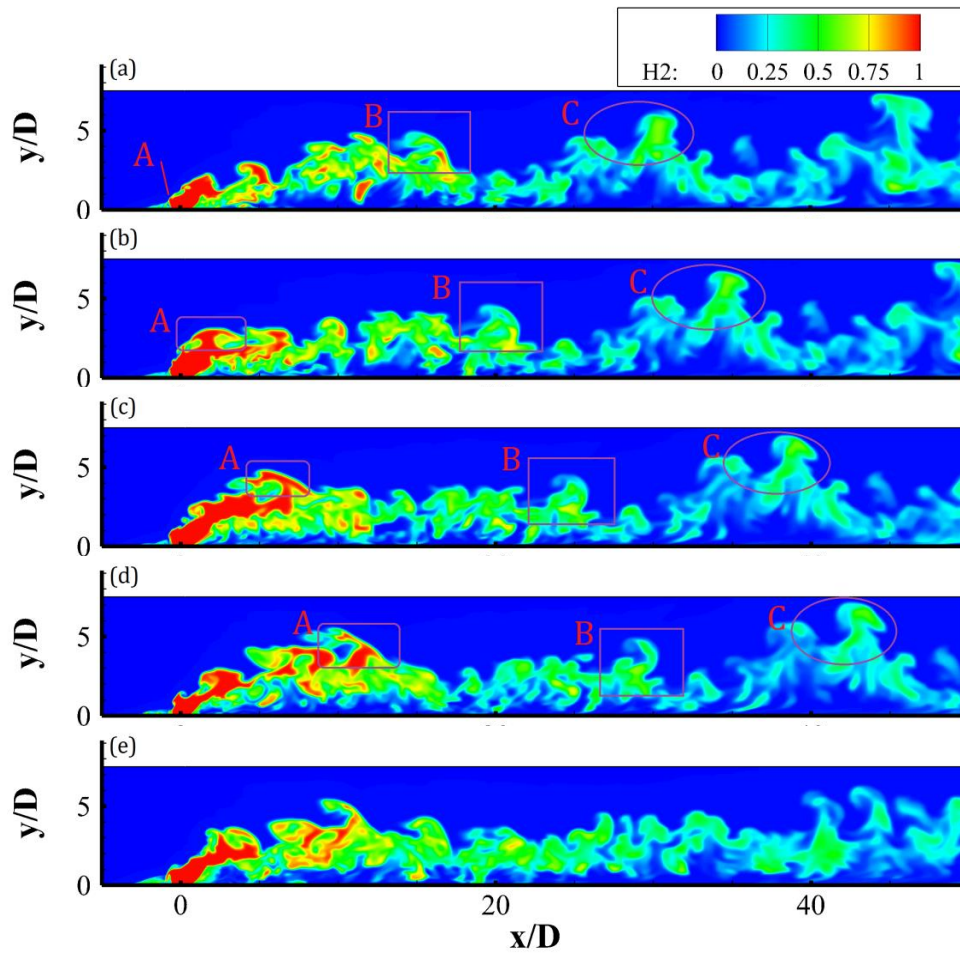
Fig. 8 Distributions of H_2 mass fraction in the central lane ($z/D = 0$) for pulsed jet and steady jet: (a) $0/4T_0$, (b) $1/4T_0$, (c) $2/4T_0$, (d) $3/4T_0$ and (e) steady jet.
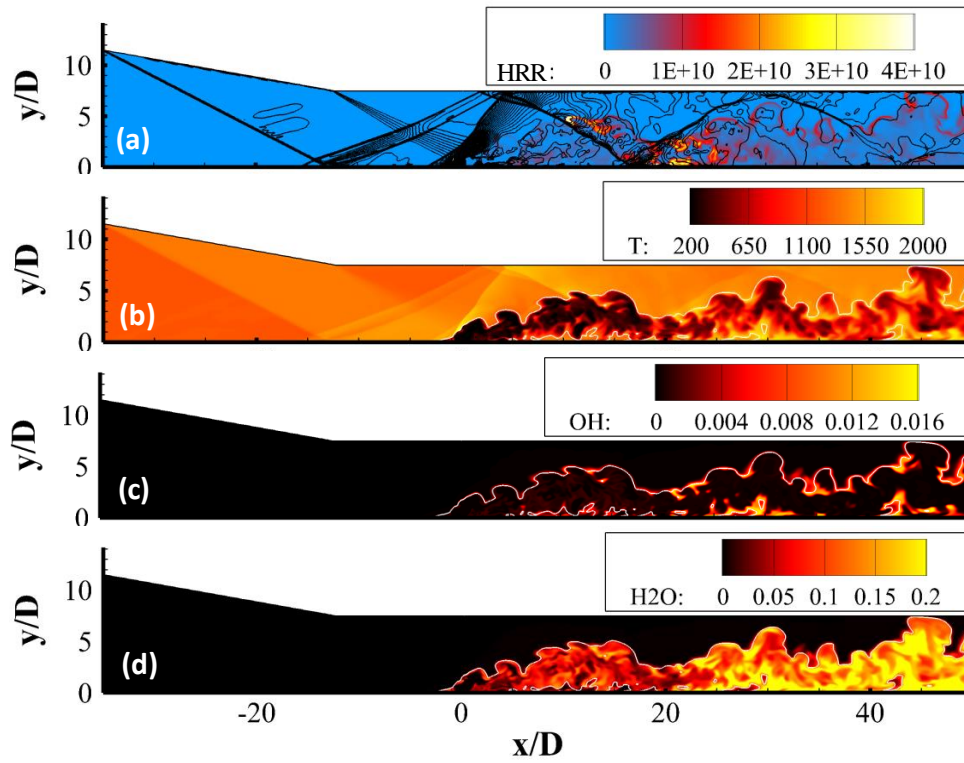
Fig. 9 Distributions of (a) HRR (J/m³/s) and pressure lined-contours (20 - 800 kPa), (b) temperature (K), mass fraction of (c) OH and (d) H_2O in the central plane (z/D = 0) at 0/4T_0.
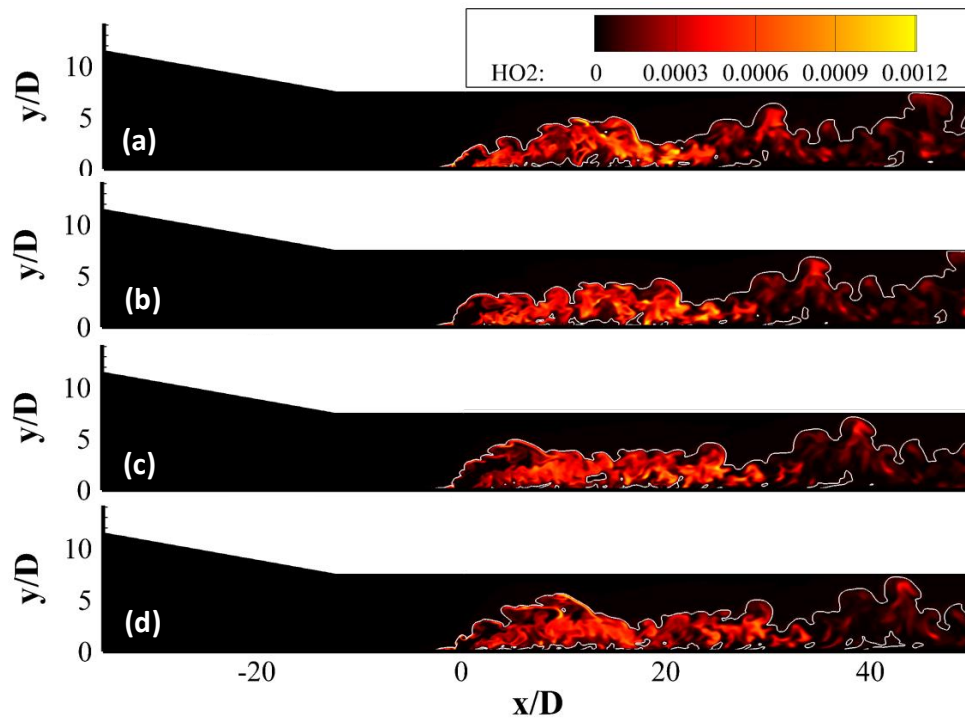
Fig. 10 Distributions of HO_2 mass fraction in the central plane ($z/D = 0$), with the white stoichiometric line (a) $0/4T_0$, (b) $1/4T_0$, (c) $2/4T_0$ and (d) $3/4T_0$.
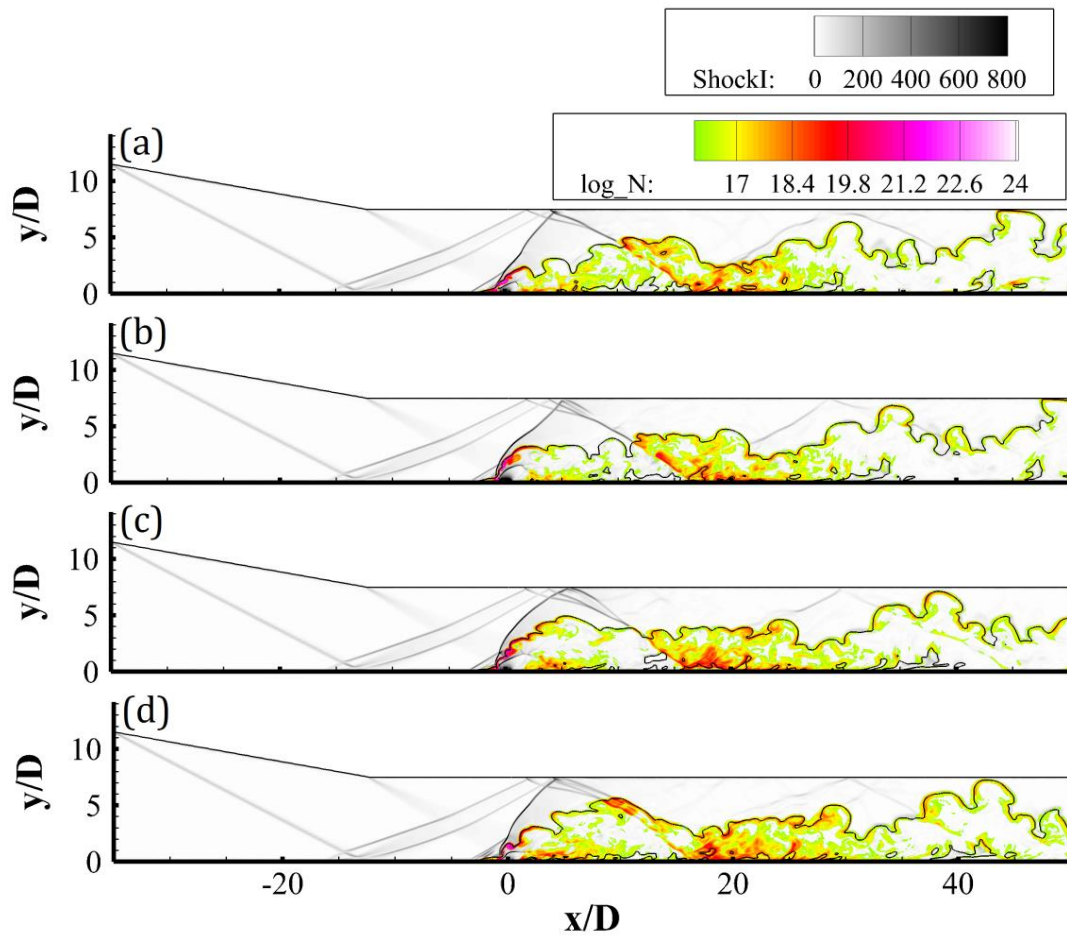
Fig. 11 Numerical schlieren results and logarithmic distributions of the index N in the central plane ($z/D = 0$), with the dark stoichiometric line (a) $0/4T_0$, (b) $1/4T_0$, (c) $2/4T_0$ and (d) $3/4T_0$.
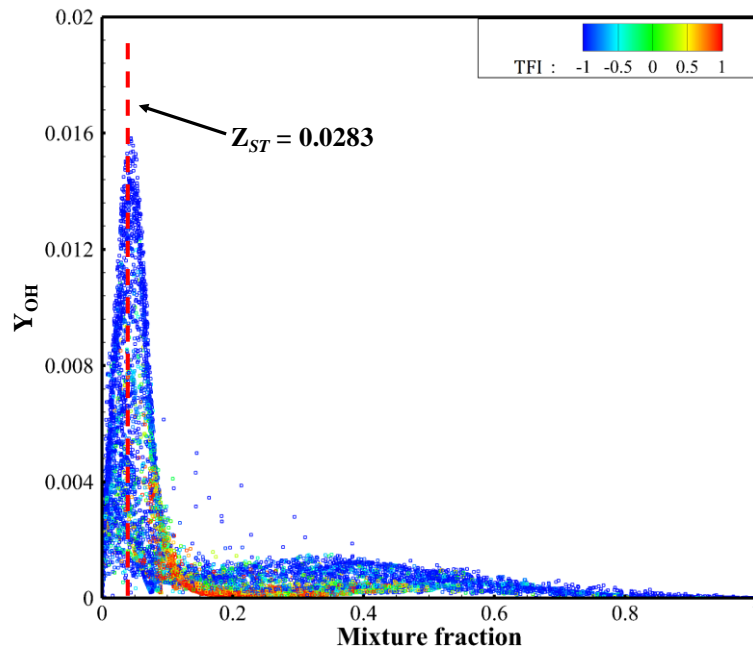
Fig. 12 The scatter distribution of the OH mass fraction coloured by TFI in the mixture fraction space on the central plane at $0/4T_0$. Dashed line: stoichiometric mixture fraction.
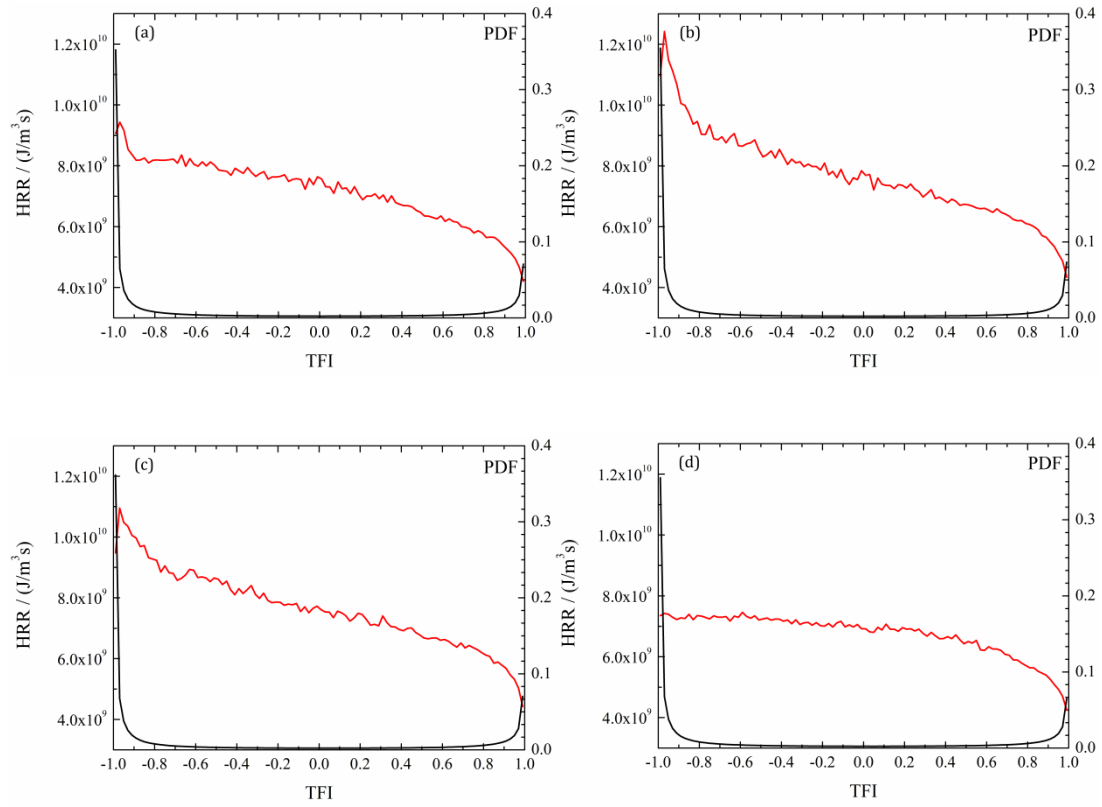
Fig. 13 Pdf of the conditional average TFI (dark line) and HRR (red line): (a) $0/4T_0$, (b) $1/4T_0$, (c) $2/4T_0$ and (d) $3/4T_0$.
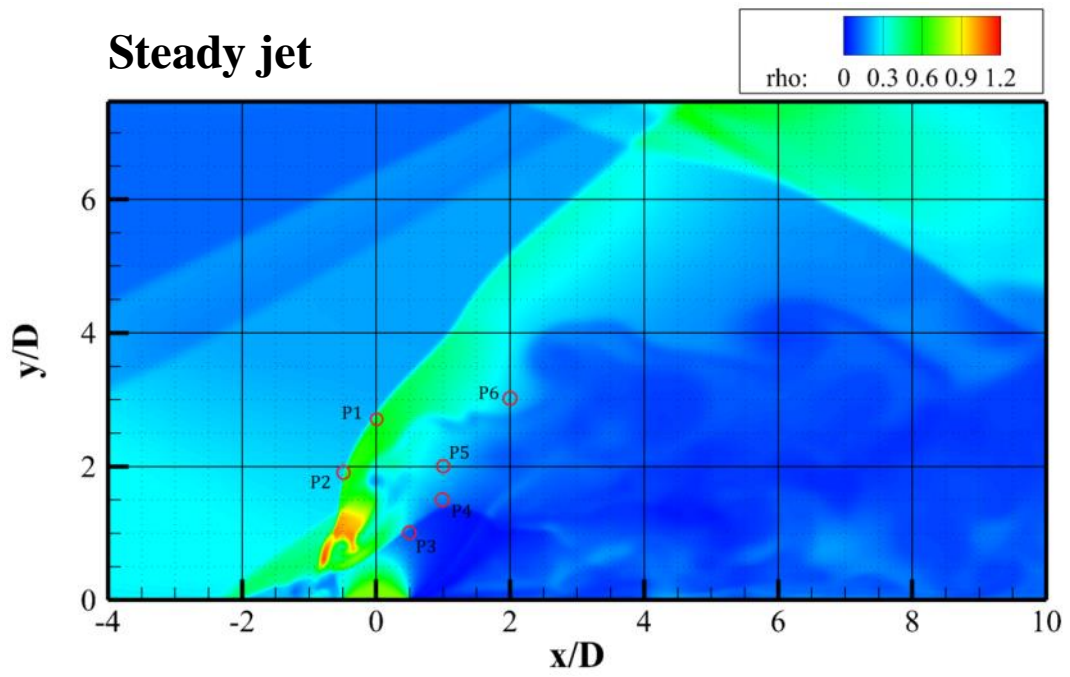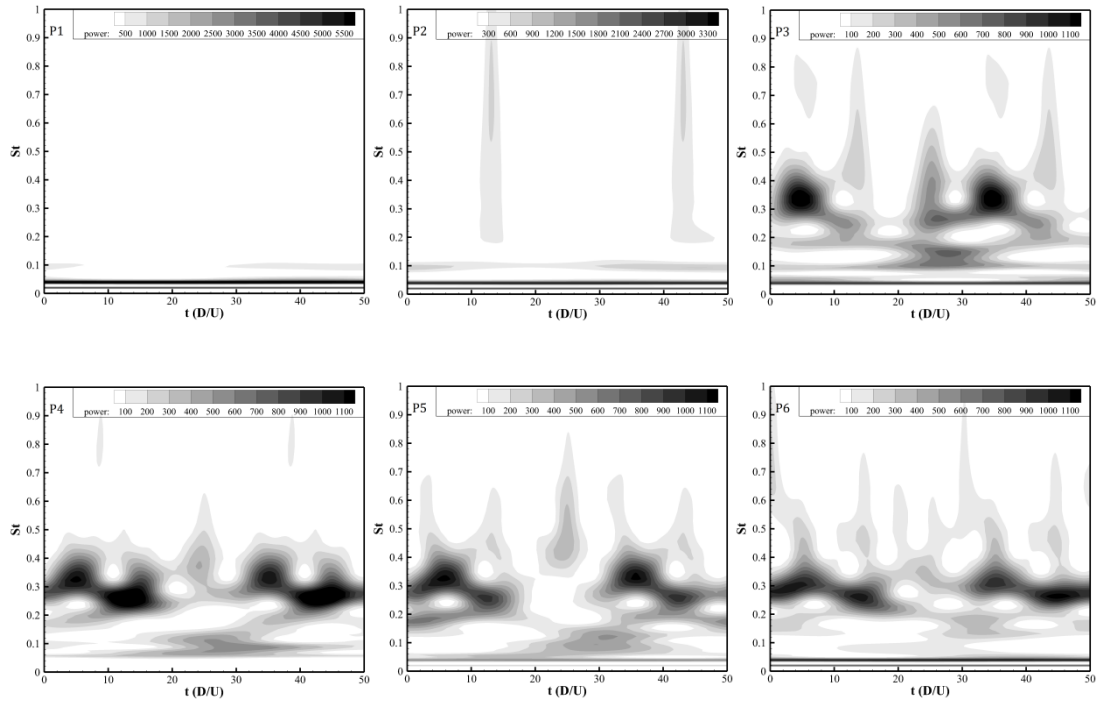
Fig. 14 Density distribution of the steady jet and the spatial positions for the PSD analysis.
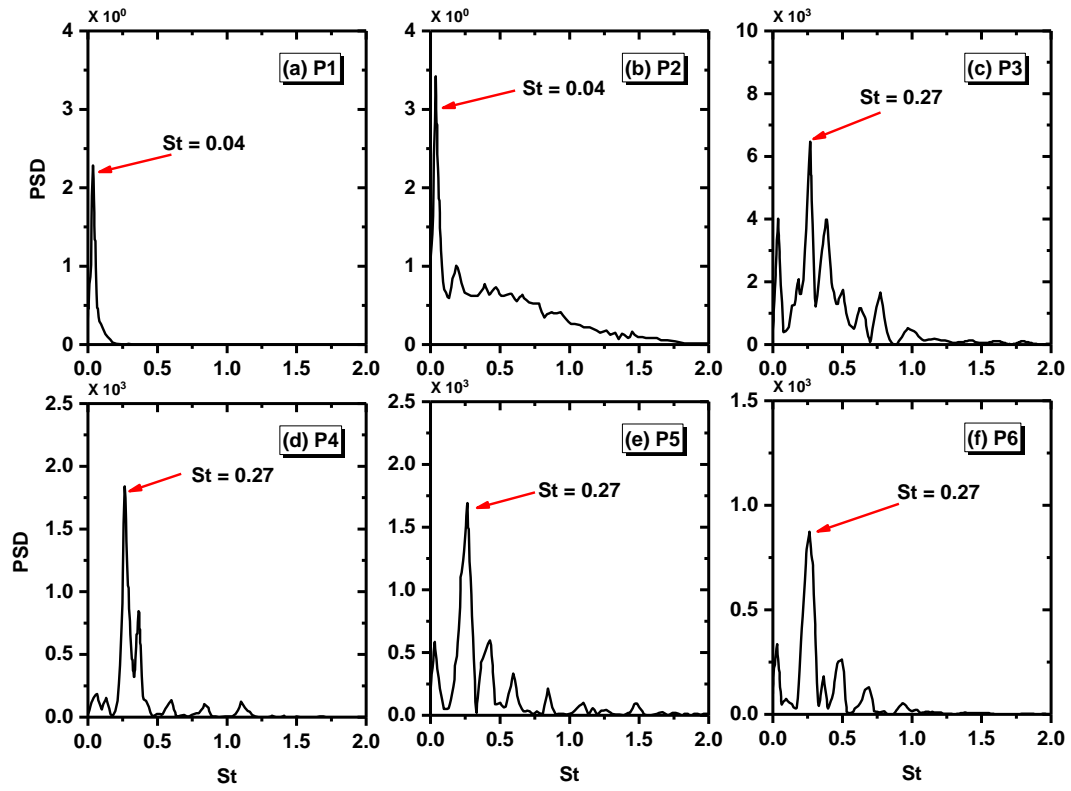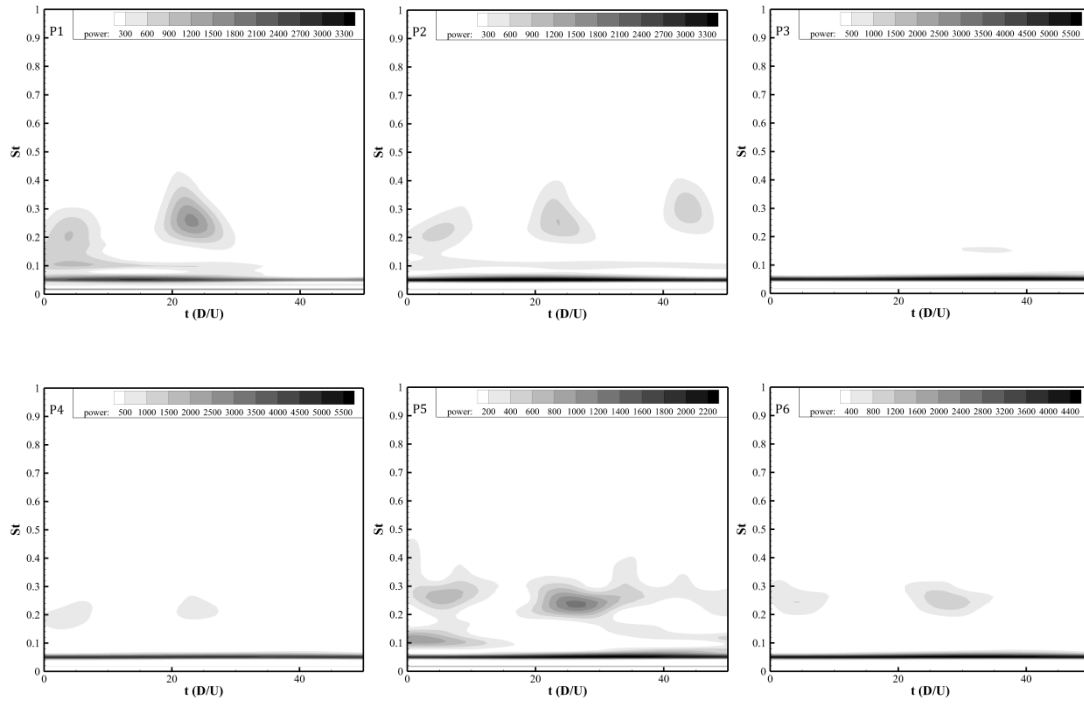
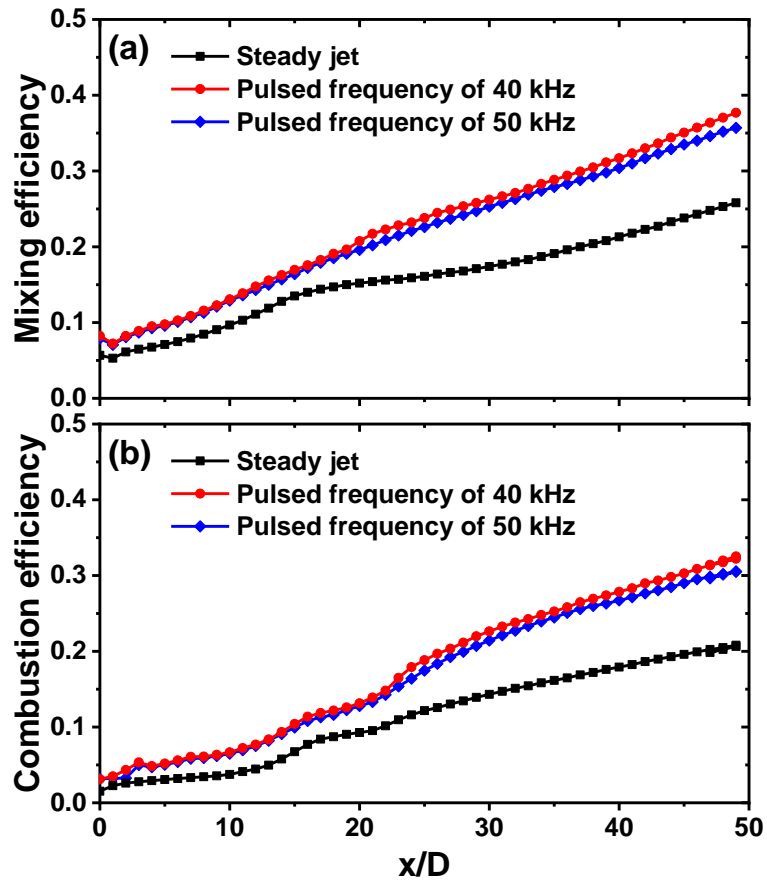**Fig. 15** St results of steady jet in supersonic cross-flow.
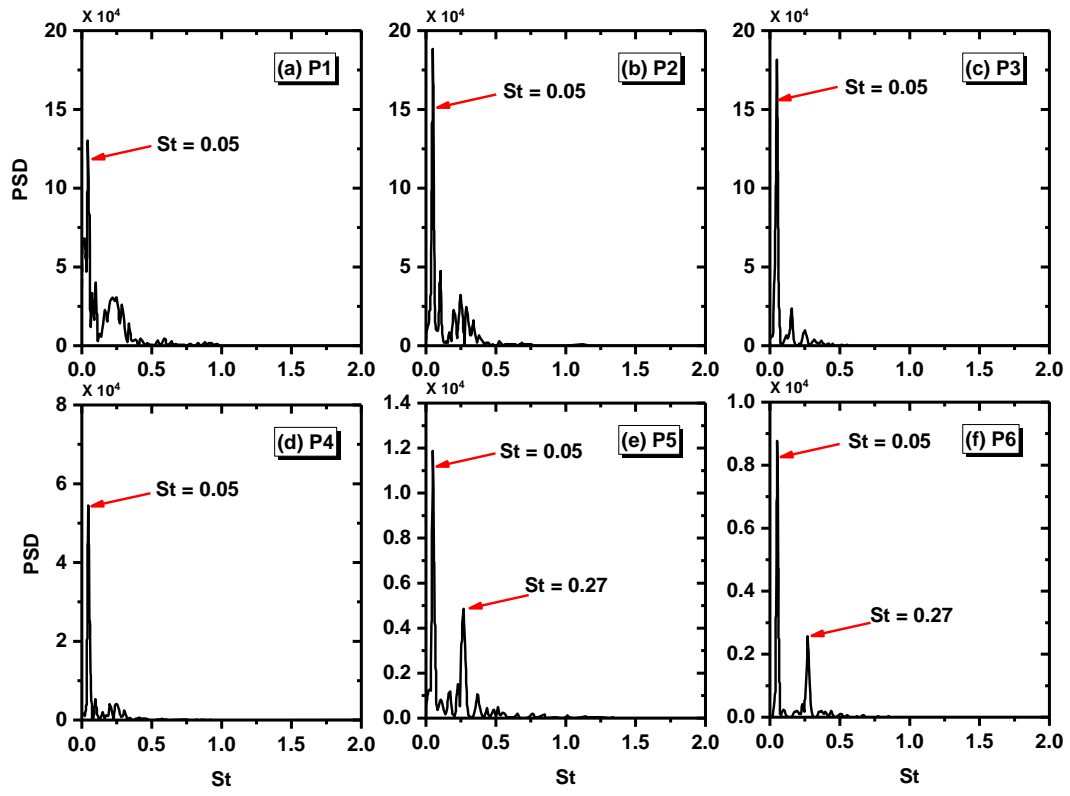
Fig. 16 St results of pulsed jet in supersonic cross-flow.

Fig. 17 Wavelet analysis of steady jet in supersonic cross-flow.

Fig. 18 Wavelet analysis of pulsed jet in supersonic cross-flow.

Fig. 19 (a) Mixing efficiency and (b) combustion efficiency from the URANS simulations.